Temperature effects on the electronic properties of lead telluride (PbTe) and the influence of nano-size precipitates on the performance of thermoelectric materials. (SrTe precipitates in PbTe bulk material – DFT study)

Sarankumar Venkatapathi

Thesis submitted to the faculty of the Virginia Polytechnic Institute and State University in partial fulfillment of the requirements for the degree of

Master of Science

in

Mechanical Engineering

Céline Hin, Chair

Scott Huxtable

Michael R.von Spakovsky

June 26, 2013

Blacksburg, Virginia

Keywords: First-principles calculations, charge carrier effective mass, scattering relaxation time, semiconductor band alignment, interface energy

Temperature effects on the electronic properties of lead telluride (PbTe) and the influence of nano-size precipitates on the performance of thermoelectric materials. (SrTe precipitates in PbTe bulk material – DFT study)

Sarankumar Venkatapathi

ABSTRACT

This study seeks to evaluate the temperature effects on the electronic properties of thermoelectric materials, using first principles Density Functional Theory (DFT) calculations by incorporating the temperature effects on structural properties of the material. Using the electronic properties attained, the charge carrier scattering relaxation times were determined. The effect of interface between PbTe and SrTe on the charge carrier mobility was studied by finding out the relative alignment of energy bands at the semiconductor heterojunction. The crystal shape of the SrTe precipitates in the PbTe host matrix was evaluated from the interface energies using the Wulffman construction. We also attempted to develop a relation between the interface energies and electronic band alignment for different interface orientations.

In this research, we incorporated the temperature effects on the structural properties of PbTe to get the temperature dependence of electronic properties like energy bandgap and effective masses of charge carriers. We used the values of bandgap and effective masses to determine the charge carrier scattering relaxation time at different temperatures which is used in evaluating the transport properties of thermoelectric materials like the Seebeck coefficient and electrical conductivity.

To my family, friends and teachers …

ACKNOWLEDGEMENT

My thesis would not have been possible without the encouragement, the technical inputs, the guidance and collaboration that were offered to me by my colleagues, friends and family. I owe my gratitude to all the people who were involved directly or indirectly in successful completion of my Master's degree. Firstly, I would like to thank my advisor, Dr. Céline Hin for her constant guidance and support. She has been my go-to person for all my queries and doubts. She has invested her valuable time in providing me with the necessary feedback which facilitated the entire research process. Her enthusiasm, her technical knowledge and her cheerful persona have motivated me to better myself, not only as a researcher, but also as an individual. I have learnt a lot under her guidance in the past couple of years.

I would like to extend a heartfelt gratitude to Dr. Scott Huxtable and Dr. Michael R.von Spakovsky for agreeing to serve as my committee members and for taking time to get to know about my research work despite their busy schedules. As a student in their graduate classes as well as through interactions with them on a personal basis, I have been able to broaden the depth of my understanding with regard many a concepts of mechanical engineering. Their expertise and constructive criticism through the process have helped me better my work, over time.

The acknowledgement would be incomplete without the mention of my colleagues and friends at Virginia Tech. I would particularly like to thank Dr. David F.Cox, Dr. Chenggang Tao, Dr. Jean Joseph Heremans, Dr. Kyungwha Park and Dr. Diana Farkas for the useful and stimulating discussions. I would like to thank the Advanced Research Computing (ARC) at Virginia Tech for allowing me to use the computational resources to successfully complete my research work. Last but not the least; I would like to thank my parents for always being there for me and for their continued belief in my work.

TABLE OF CONTENTS

LIST OF FIGURES

LIST OF TABLES

1 Introduction

Energy, which is the backbone of our modern world, has become very essential for human survival and to sustain the quality of human life. It comes with a high economic, social and environmental cost which is likely to increase in the future because of expanding energy demands, limited availability of fossil fuel resources, environmental impact of global warming and need for increased fuel efficiency. The solution to energy crisis is to search for sustainable energy sources and effective use of available energy resources. One of the practicable solutions is the use of thermoelectric generators in various applications. These types of power generators could be used along with many energy conversion devices where there is significant heat generation during the conversion process. Recent developments in nanotechnology and band structure engineering have led to renewed interest in this area. It is expected that thermoelectric phenomena, which involves the conversion between thermal and electrical energy, will play an important role in global sustainable energy solution.

1.1 Thermoelectric materials

Thermoelectric materials are a class of materials, which employ the direct conversion of thermal to electrical energy using solid-state energy conversion.

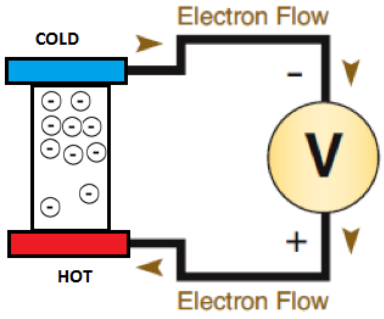

Figure 1.1: Schematic representation of thermoelectric phenomenon

Thermoelectric devices provide attractive advantages over many of the other conventional energy conversion modules by allowing flexibility in operation, lack of moving parts, high reliability, scalability and long life [1]. This technology finds several applications in space power generation and through scavenging of waste heat generated from automobile exhausts, air conditioning systems and other industrial processes [2]. Thermoelectric materials can also be used in solid-state Peltier coolers to replace the compression-based refrigeration, which has the tendency to release harmful gases that affect the atmosphere [3]. In heating and cooling applications thermoelectric materials have a good temperature control because the same module can be used for both heating and cooling which is totally dependent on the direction of current flow.

Thermoelectric devices are, in general, made from thermoelectric modules. A thermoelectric module is an array of thermocouples connected electrically in series but thermally in parallel [4]. In spite of the several advantages cited above, these thermoelectric devices are not popular because they are too inefficient to be cost effective. Two basic modes of thermoelectric device are shown in Fig. 1.2 [5].

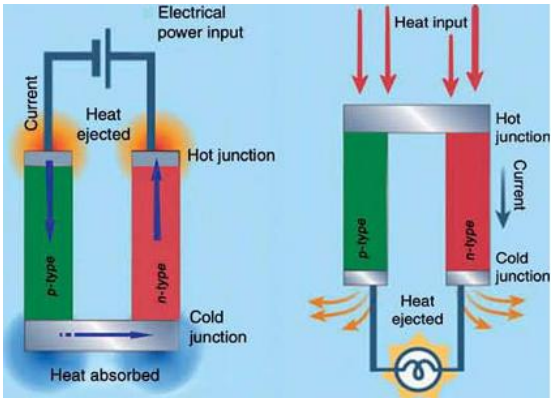

Figure 1.2: Two basic modes of thermoelectric device (a) Thermoelectric refrigeration (b) Thermoelectric generation.

The performance of these materials is characterized by a dimensionless material property called the thermoelectric figure of merit (zT), which is a combination of interrelated thermoelectric properties like the Seebeck coefficient (α) , electrical conductivity (σ) and thermal conductivity (κ). The expression for figure of merit is given by,

$$zT = \frac{\alpha^2 \sigma\, T}{\kappa};\ \kappa = \kappa_{lattice} + \kappa_{electronic}$$

where α is the Seebeck coefficient (V/K), T is the temperature (K), σ is the electrical conductivity (S/m), κ is the total thermal conductivity (W/m-K), $\kappa_{lattice}$ is the lattice thermal conductivity (W/m-K), $\kappa_{electronic}$ is the electronic thermal conductivity (W/m-K) and $\alpha^2\sigma$ is the power factor.

Traditional heat engines operate in the range of Carnot efficiencies of 30-40%. These ranges take into account the immense heat loss from the heat engines to the surroundings during the energy conversion process. Improving the overall heat to electrical conversion would have a great impact on the total energy utilization [4]. However, these losses can be negated to an extent by incorporating thermoelectric generators in the energy conversion system. Thermoelectric materials use the waste heat generated and convert it to useful electricity. Thermoelectric generators can be viewed as heat engines where the electron gas is the working fluid.

With the assumption of free electron gas as the working fluid and the thermoelectric material operates between two constant temperature sources T_{hot} and T_{cold} generating power output, the efficiency of this reversible thermodynamic cycle is given by Carnot's efficiency (η_C)

$$\eta_C = \frac{T_{hot} - T_{cold}}{T_{hot}}$$

But in reality, the efficiency of thermoelectric materials is limited by the irreversible processes like finite thermal conductivity of the material. For small temperature differences the maximum device efficiency (η) of thermoelectric material is given by [4],

$$\eta = \frac{\Delta T}{T_{hot}} \frac{\sqrt{1+zT}-1}{\sqrt{1+zT}+1}$$

$\Delta T = T_{hot} - T_{cold}$ is the temperature difference (K) , T_{hot} is the hot side temperature (K) and zT is the figure of merit. We could see that the maximum device efficiency is limited to a fraction of Carnot's efficiency through the figure of merit. Values of zT around 1 are considered to be good, but in order to achieve commercial viability in a market dominated by heat engines, one expects values of zT around 3–4 for thermoelectric material based devices [6].

The existing thermoelectric materials have not been found to have a zT greater than 2.2 [7]. A higher zT is difficult to achieve because of the conflicting nature of the interrelated thermoelectric properties.

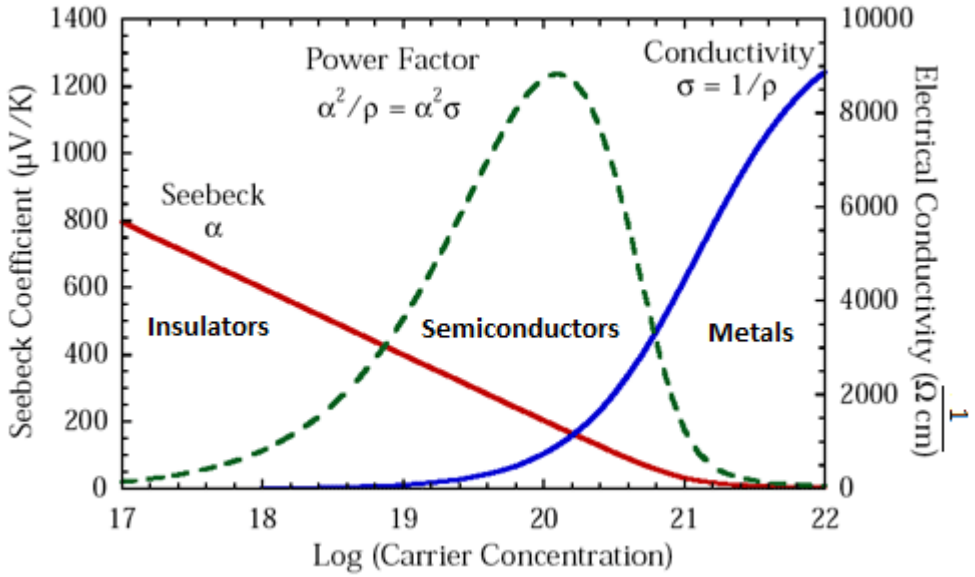

Figure 1.3: Interrelated thermoelectric properties vs. carrier concentration.

Fig. 1.3 [4] shows the trend in thermoelectric properties versus the carrier concentration, we can see that as the carrier concentration increases, the Seebeck coefficient decreases and the electrical conductivity increases. The two ways to improve the figure of merit (zT), are either by decreasing the thermal conductivity or by increasing the power factor. In order to have high value of figure of merit, it is necessary to reach an optimal value for both Seebeck coefficient and electrical conductivity which peaks in the region of carrier concentration which pertains to that of semiconductors. Thus, the interrelated properties make it difficult to increase zT in a material. Good thermoelectric materials are typically heavily doped semiconductors with carrier concentration of 10^{19} to 10^{21} carriers/cm^3 (depending on the material system) [4].

The temperature range that optimizes the figure of merit categorizes the thermoelectric materials into three groups; low temperature materials (up to 450K) consisting of Bi_2Te_3 and its alloys ($E_g = 0.16\ at\ 300\ K$), the intermediate (450 – 850K) range consisting of $PbTe$ and its alloys ($E_g = 0.33\ at\ 300\ K$) and high temperature materials (up to 1300 K) comprising of $SiGe$ and its alloys ($E_g = 1.02\ at\ 300\ K$).

The operating temperature ranges for thermoelectric materials are decided by the energy bandgap (E_g), a material property. Low bandgap semiconductors are good thermoelectric materials at low temperatures, when operated in high temperature regimes, more charge carriers can easily be excited and this leads to an increase in the thermal conductivity of the materials which is undesirable for the performance of thermoelectric materials.

1.2 Engineering thermoelectric materials

The three main variables that need to be engineered are Seebeck coefficient, electrical conductivity and thermal conductivity. Thermal conductivity in these materials is established by two modes of heat transport. Phonons travelling through the crystal lattice transport heat and lead

to lattice thermal conductivity. The electrons (or holes) also transport heat and lead to the electronic thermal conductivity, but in semiconductors, its contribution is very small and is mostly neglected.

The lattice part of thermal conductivity is an independent property and it can be lowered in nanostructured materials with fine grain sizes that can scatter the phonons [4]. The increase of power factor is a challenging task since Seebeck coefficient decreases and electrical conductivity increases as a function of carrier concentration.

The expressions for Seebeck coefficient (α) and electrical conductivity (σ) in terms of carrier concentration (n), effective mass (m^*), charge carrier scattering relaxation time (τ) and carrier mobility (μ) are given as follows:

$$\alpha = \frac{8\pi^2 k_B^2}{3eh^2} m^* T \left(\frac{\pi}{3n}\right)^{2/3}$$

$$\sigma = ne\mu \ ; \ \mu = \frac{e\tau}{m^*}$$

Effective masses of the carriers and carrier concentrations provide a trade-off as large effective mass and small carrier concentration provide large thermopower (Seebeck coefficient), but low electrical conductivity due to reduced carrier mobility [8].

1.3 Research objective

Advancements in material sciences present opportunities to improve the figure of merit in thermoelectric materials. This particular study seeks to investigate the extent of improvement in the performance of lead telluride material in the presence of nano size SrTe precipitates.

In nanostructured bulk materials the fine grains of the materials, as well as the grain boundaries, are the sources for phonon scattering. This phonon scattering reduces the thermal conductivity of the material. An additional decrease of the thermal conductivity could be possible by having

precipitates of different materials in the host thermoelectric material so that there could be additional phonon scattering at the interfaces along with finer grain boundary scattering. A challenge in this regard is that very fine grain size of the thermoelectric material and the presence of many interfaces may affect the mobility of charge carriers by scattering the electrons along with phonons at the boundaries and interfaces, thus reducing the electrical conductivity. Given the conflicting characteristics of the properties, it is necessary to achieve the optimal doping concentration in the thermoelectric host material. Thus, it is imperative to find a material which enables phonon scattering, with minimal affect on mobility of charge carriers. One such material that seems to fit these criteria is $Pb_{1-x}Sr_xTe$ alloys [9]. The broader objective of this research is to work on PbTe thermoelectric material and determine the effect of nano-size SrTe precipitates on the charge carrier mobility and hence on the thermoelectric performance, which could be improved in order to achieve commercial viability.

Previous research studies on this material indicate that doping of PbTe with Tl led to enhanced zT of 1.5 at 773 K [10]. Also, Na doped PbTe achieved zT values of 1.4 at 753K [11]. Our study delves into the understanding of the electron mobility at the interfaces by relating it to the band alignment at the semiconductor junction. It is experimentally found that the addition of Sr in PbTe triggers the formation of SrTe nano crystals in the host matrix and a high zT of 1.7 is achieved at 800 K [9] and 2.2 at 915 K [12].

1.4 Research tasks

We could say that there are possibilities to enhance zT by not only reducing the thermal conductivity, but also by improving the power factor, which could be understood from the expression that relates zT and the thermoelectric properties. In this work we focus on improving the power factor of $Pb_{1-x}Sr_xTe$ alloy by studying the band alignment at the semiconductor

heterojunction using first principles calculations. In this Masters research work; initially the electronic properties of PbTe are determined at different temperatures from first principles Density Functional Theory (DFT) calculations by incorporating the temperature effects on the structural properties. The obtained property values were used in the mathematical models that were developed to evaluate the charge carrier scattering time at different temperatures. At the next phase, we determined the interface energies between PbTe and SrTe to understand the influence of SrTe precipitates on the charge carrier mobility in PbTe material. This was achieved by studying the band alignment between PbTe and SrTe semiconductor heterojunction. Finally, we used the interface energies from different orientations to get the equilibrium shape of SrTe precipitates in the PbTe host matrix.

1.5 References

1. A. Majumdar, Thermoelectricity in semiconductor nanostructures. *Science* **303**, 777 – 778 (2004).
2. http://voyager.jpl.nasa.gov/spacecraft/spacecraftlife.html
3. Y. Cui, Thermoelectric materials: Ternary and Higher oxides and Telluride. Canada (2009).
4. http://www.thermoelectrics.caltech.edu/thermoelectrics/engineering.html
5. http://blogs.cas.suffolk.edu/anestisrealm/2011/10/30/toms-mystic-devices/
6. F.J. DiSalvo, Thermoelectric cooling and power generation. *Science* **285**, 703 – 706 (1999).
7. http://www.mccormick.northwestern.edu/news/articles/2012/09/vinayak-dravid-thermoelectric-material-world-record.html
8. D.M. Rowe, Thermoelectric Handbook. CRC Press, Boca Raton (2006).
9. K. Biswas, J. He, Q. Zhang, G. Wang, C. Uher, V.P. Dravid, M.G. Kanatzidis, Strained endotaxial nanostructures with high thermoelectric figure of merit. *Nature Chemistry* **3**, 160 – 166 (2011).
10. J.P. Heremans, V. Jovovic, E.S. Toberer, A. Saramat, K. Kurosaki, A. Charoenphakdee, S. Yamanaka, G.J. Snyder, Enhancement of Thermoelectric efficiency in PbTe by distortion of the electronic density of states. *Science* **321**, 554 – 557 (2008).
11. Y. Pei, A. LaLonde, S. Iwanaga, G.J. Snyder, High thermoelectric figure of merit in heavy hole dominated PbTe. *Energy Environ. Sci*. **4**, 2085 – 2089 (2011).
12. K. Biswas, J. He, I.D. Blum, C.I. Wu, T.P. Hogan, D.N. Seidman, V.P. Dravid, M.G. Kanatzidis, High – performance bulk thermoelectric with all – scale hierarchical architectures. *Nature* **489**, 414 – 418 (2012).

2 Background and literature review

This chapter on thermoelectric background and literature review is broadly divided into two sections. The first segment outlines the thermoelectric phenomena, gives a brief description of thermoelectric properties and the factors influencing the performance of thermoelectric materials. The latter half of the chapter deals with the prior research work done on bulk thermoelectric materials that focus on altering the thermoelectric properties to enhance their performance. It also deals with the current developments in nanostructured bulk thermoelectric materials.

2.1 Thermoelectric phenomenon

The thermoelectric effect is the direct conversion of temperature gradient to voltage potential gradient and vice-versa. From the discussion in the previous chapter we know that the efficiency of thermoelectric materials is characterized by the dimensionless figure of merit (zT) which is a function of Seebeck coefficient, electrical conductivity and thermal conductivity. Here we discuss each of these properties in detail.

2.2 Seebeck effect

It was observed by Thomas John Seebeck in 1821, that when a temperature gradient (ΔT) was established in a material, conducting charge carriers diffuse from the hot side (high energy region) to the cold side (low energy region) and create the electrical voltage potential difference (ΔV) across the material. The voltage potential gradient is directly proportional to the temperature differences across the material and the proportionality constant is defined as Seebeck coefficient (α).

$$\alpha = -\frac{\Delta V}{\Delta T}$$

Seebeck coefficient is either positive or negative depending on the majority charge carriers (holes or electrons) in the material under consideration. The schematic representation of Seebeck effect is shown in Fig. 2.1,

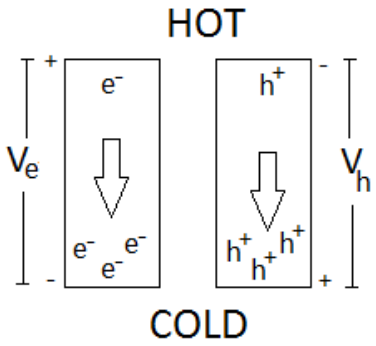

Figure 2.1: A schematic representation of Seebeck effect

The thermoelectric properties, also known as transport properties, depend on the carrier concentration in the material of concern. Hence, it is vital to study the electronic structure of thermoelectric materials. The different transport properties that are involved in determining the zT of the material are discussed here.

2.3 Seebeck coefficient

Seebeck coefficient is a transport property that can be measured as a ratio of potential difference and temperature difference across the material. It is a material property and is independent of the geometry of the material. For large Seebeck coefficients in a material, there should be only one type of charge carriers (either holes or electrons) because mixed conduction would lead to cancelling out of induced voltage [1]. The Seebeck coefficient (α) is related to carrier concentration (n) and effective mass of the carrier (m^*) through the following expression,

$$\alpha = \frac{8\pi^2 k_B^2}{3eh^2} m^* T \left(\frac{\pi}{3n}\right)^{2/3}$$

where k_B is the Boltzmann's constant, e is the charge of carrier, h is the Planck's constant and T is the temperature

2.4 Electrical conductivity

Electrical conductivity is the phenomenon observed in a material when it is subjected to an external electric field. The randomly moving electrons of the constituting atoms of the material will experience a force and this applied electric field (E) will give the random motion a net drift velocity (v) in one direction. The average drift velocity depends on the effective mass (m^*) of the electron and the charge carrier scattering relaxation time (τ). The expression for drift velocity can be derived from Newton's laws of motion as,

$$v = \frac{eE\tau}{m^*}$$

For n electrons per unit volume of a material with charge e, moving with a drift velocity v along the direction of the applied electric field E, the current flux or the electron flux j is given by,

$$j = nev; \;\; j = \sigma E$$

The electron flux is directly proportional to the applied electric field and the proportionality is the electrical conductivity (σ) which is again a material property. Furthermore, the electron mobility μ is defined as the ratio of average drift velocity to the applied field and from which we get the electrical conductivity in terms of carrier concentration (n) and effective mass of the carrier (m^*) as,

$$\sigma = ne\mu \; ; \qquad \mu = \frac{e\tau}{m^*}$$

2.5 Thermal conductivity

Thermal conductivity is a property of the material and is a measure of the ability of the material to conduct heat. The heat transfer or heat flux through the material is directly proportional to the temperature gradient across the material, and the governing equation is given by Fourier's law,

$$q = -\kappa \, \Delta T$$

The proportionality constant is the thermal conductivity (κ) of the material. The thermal conductivity of the material can be expressed as a sum of lattice and electronic thermal conductivities as shown in the equation.

$$\kappa = \kappa_{lattice} + \kappa_{electronic}$$

2.6 Electronic thermal conductivity

The assumption of electrons as classical particles in a solid, gives the energy of electron at temperature T as, $\frac{3}{2}k_B T$. When there is a temperature gradient across the material, electrons drift towards the colder side and using the expressions for drift force in terms of scattering time and drift velocity from electrical conductivity, we can express the electronic thermal conductivity in terms of electrical conductivity as,

$$\kappa_{electronic} = L_0 \sigma T; \quad L_0 = \frac{3}{2}\left(\frac{k_B}{e}\right)^2 \qquad where\ L_0\ is\ the\ Lorenz\ number$$

From the relation we could see that the ratio of electronic thermal conductivity to electrical conductivity of the material is directly proportional to the temperature. This is known as Wiedemann-Franz law. The electronic part of thermal conductivity is significant in metals because of the presence of free conduction electrons due to partially filled bands that primarily transport heat across the material, and it is usually negligible in semiconductors and insulators at

low temperatures because there are no free electrons since all the electronic bands are fully occupied.

2.7 Lattice thermal conductivity

At significant temperatures, the atoms in a crystal undergo vibrations because of thermal energy. The energy transmission through uniform vibrations of the atoms in a solid can be envisaged as the propagation of sound waves through the material. These are called phonons, and they have both energy and momentum, hence they can transport energy in the form of heat. This leads to the lattice part of the thermal conductivity of the material. These heat carrying waves, travel with the speed of sound and they are scattered by different mechanisms, hence leading to a finite thermal conductivity of the material. The expression for the lattice part of thermal conductivity is given by Debye's model,

$$\kappa_{lattice} = \frac{1}{3} C_v v_{ph} l_{ph}$$

The lattice part of thermal conductivity depends on the specific heat at constant volume of the material (C_v), average phonon mean free path (l_{ph}) and the average phonon velocity (v_{ph}) inside the material. This mode of heat transport is prominent in semiconductors and insulators.

Thus, from the above expressions for transport properties, we could see that the transport properties are all related through carrier concentration. Materials with short scattering times and large effective masses exhibit low electrical conductivities. The exact relation between effective masses and mobility is complex and it depends on multiple factors like electronic structure, scattering mechanisms and anisotropy of the material [3].

The temperature dependence of electrical conductivity is from effective mass and carrier concentration. Electrical conductivity and electronic thermal conductivity are related by Wiedemann-Franz law. The electrical conductivity increases with increase in temperature as the

carrier concentration increases with temperature. The Seebeck coefficient is higher when the effective mass of the carriers are large and carrier concentration levels are low. Metals have high electrical conductivities and relatively low Seebeck coefficients, the electronic thermal conductivity is also high, and hence it is difficult to realize high zT in them. Similarly in the case of insulators, the electrical conductivity is very low, leaving the semiconductors as the best zT available materials.

The next section focuses on the prior work and current progress in nanostructured bulk thermoelectric materials. The research work on improving the efficiency of thermoelectric materials could be broadly classified based on the experimental and theoretical work done in that area.

2.8 Experimental work

It was experimentally observed by Simon et al. [2] that PbTe forms local structural dipoles from undistorted rock salt structure. It was found that the off centering of Pb^{2+} ions (atomic displacements) were higher when compared to the Te^{2-} ions and the temperature dependence of lattice parameter and the above mentioned atomic displacement parameter were linear. The refined distortion saturated at a maximum value of 0.24 Å and there was no change in crystal symmetry at approximately 450 K. It was believed that these structural effects would explain the linear temperature dependence of energy bandgap, very low lattice thermal conductivity at high temperatures and strong temperature dependence of charge carrier scattering [2].

The recent advancements in thermoelectric materials are because of developments of new concepts in nanotechnology to engineer the electron and phonon transport in the material. Based on the discussion from the previous section, the thermal conductivity in semiconductors is primarily due to phonon heat transport. The other thermoelectric properties depend on the

electron transport across the material and the lattice part of thermal conductivity primarily depends on phonons. This lattice thermal conductivity could be reduced by effectively scattering the phonons by nanostructuring and alloying the materials [3].

Various techniques through which the scattering of phonons is achieved are grain size reduction in materials, and production of finer microstructure by using nanocomposites with two or more phases [3]. The presence of nanoparticles in conjunction with many grain boundaries in a material provides an effective scattering mechanism for mid/long wavelength phonons that dominate heat conduction and contribute to the lattice thermal conductivity [3].

A new class of materials was developed by Dresselhaus et al. [4] called as phonon–glass/electron–crystal (PGEC) materials. These materials act as glass with regards to thermal conductivity and simultaneously as a crystal for electrical conductivity. PGEC materials have interstitial atoms in the empty spaces of host material whose vibrations are asynchronous with the host atoms and thus scatter the phonons, which contributes to the lattice thermal conductivity of the material [5]. zT improvements due to low thermal conductivity were also observed in nanocrystalline bulk BiSbTe materials. The reduction in thermal conductivity is due to the increased phonon scattering by grain boundaries and defects in the material. An increased zT of around 1.4 was achieved at 373 K making these materials useful at room temperature cooling and power generation applications.

Similar work was done on PbTe alloys that are well known thermoelectric materials in the mid temperature range. The solubility of Cd in PbTe substrate was studied by Kanatzidis et al. [6] and it was found that the growth of CdTe nanocrystals in PbTe matrix would create nanostructuring that suppresses the lattice thermal conductivity by scattering the phonons at the interfaces and hence enhance the zT. A maximum zT of 1.2 was achieved at 720 K.

Lattice thermal conductivity of $PbTe_{0.7}S_{0.3}$ material was calculated based on transmission electron microscopy observations and a low value of thermal conductivity of $0.8 Wm^{-1}K^{-1}$ was reported at room temperature. This reduction was due to enhanced phonon scattering at phase boundaries, interfacial dislocations, and nanometer-scale PbS precipitates in the PbTe matrix [7].

In bulk materials there is a lower limit for lattice thermal conductivity. Based on wave mechanics the phonon mean free path cannot be shorter than the interatomic distance in the crystal. The minimum thermal conductivity of PbTe is about 0.35 W/mK at 300 K [8]. There is also an effect on carrier mobility because carriers are also scattered at the interfaces and grain boundaries like the phonons. Now the considerable improvements on the performance of thermoelectric materials should be by enhancing the power factor. Few research groups work on enhancing the power factor and hence the zT of bulk thermoelectric materials.

Heremans et al. [9] followed the approach of distorting the electronic density of states (DOS) of the material to increase the thermopower of the material. A local increase in the density of states over a narrow energy range near the Fermi level was achieved by doping Tl in PbTe. The local increase in DOS near the Fermi energy is shown in the Fig. 2.2 [9]. This increase is achieved when the conduction or valence band of the semiconductor resonates with one of the energy levels of a localized atom in the semiconductor material matrix.

The effective mass of the carrier is directly related to the density of states $g(E)$ as shown in the following expression,

$$g(E) = \frac{(m^*)^{3/2}\sqrt{2E}}{\pi^2 \hbar^3}$$

where m^* is the effective mass of charge carrier, E is the energy level and ħ is the modified Planck constant. An increase in the effective mass of the carriers by local increase in the density of states would enhance the Seebeck coefficient of the material. Group III elements like Ga, In,

and Tl create additional energy levels called resonant energy levels in PbTe that would lead to enhancement of density of states near the Fermi energy level E_F. The figure of merit achieved by this kind of band structure engineering in p–type PbTe is above 1.5 at 773 K [9]. This type of band structure engineering along with nanostructuring to reduce the lattice thermal conductivity would further enhance the zT of the material [9].

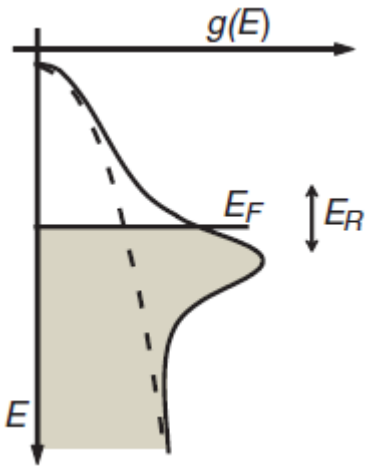

Figure 2.2: Schematic representation of DOS of valence band of pure PbTe and Tl-PbTe.

The shaded region represents the filled energy levels and E_R represents the resonant energy levels. Seebeck coefficient enhancement by density of states modification is a promising approach. It affects the carrier mobility and hence the electrical conductivity because of an increase in effective mass of the carriers. Snyder et al. [10] demonstrated a new approach in band structure engineering to enhance the power factor of thermoelectric materials by tuning the doping concentration and composition of the material. High band valley degeneracy in electronic band structure could improve the power factor and hence the zT. A high zT of 1.8 at 850 K was reported in doped $PbTe_{1-x}Se_x$ alloys. By choosing the optimal doping concentration, the density of states effective mass is improved by increasing the valley degeneracy without increasing the band effective mass (conductivity effective mass, m_b^*). The carrier mobility is unaffected by the

valley degeneracy. The relation between density of state effective mass and band effective mass is given by the following expression,

$$m^* = N_v^{2/3} m_b^*$$

In $PbTe_{0.85}Se_{0.15}$ alloy, the convergence of L and Σ valence bands increases the valley degeneracy to 16 as shown in Fig. 2.3 [10], hence enhancing the Seebeck coefficient [10].

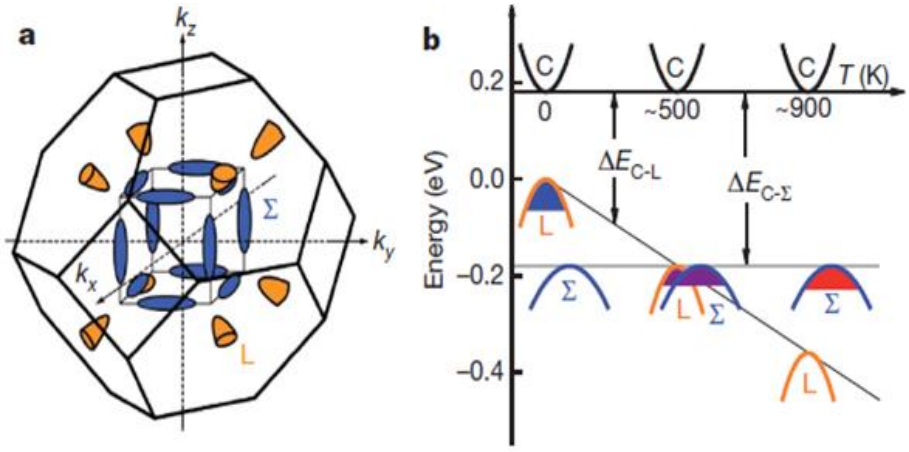

Figure 2.3: Valence band structure of $PbTe_{1-x}Se_x$ (a) Brillouin zone showing low and high degeneracy hole pockets. (b) Relative energy of valence bands, at ~500K two valence bands converge.

In $Pb_{1-x}Sr_xTe$ alloy doped with Na_2Te the presence of Sr in the PbTe host matrix forms endotaxial SrTe nanocrystals. This nanostructuring reduces the lattice thermal conductivity by scattering the phonons. Additional phonon scattering was also observed because of these nano-sized SrTe precipitates in the PbTe matrix [11]. These interfaces seem to not affect the carrier mobility because of good band alignment at the PbTe and SrTe semiconductor heterojunction leading to a high zT of around 1.7 at 800 K [11]. Nanostructuring in bulk thermoelectric materials scatter a significant portion of phonons, but phonons with very long mean-free-paths are unaffected by nano structures. These phonons could be scattered at the mesoscale grain boundaries. There is a significant increase in figure of merit from atomic scale to mesoscale scattering mechanisms. Taking advantage of all length scale scattering mechanisms like

mesoscale grain boundaries, endotaxial nanostructuring and atomic scale substitutional doping, a high zT of 2.2 is achieved in a p-type PbTe-SrTe system at 915 K. Waste heat conversions of approximately 16.5% to 20% could be achieved using these thermoelectric materials [12].

Now we focus on the theoretical methods that are employed to determine the thermoelectric performance of materials.

2.9 Theoretical work

The thermoelectric performance of the materials is characterized by both electron and phonon transport across the material. Theoretical calculations of electron and phonon transport can be done by using a multi-scale approach that includes first principles calculations, molecular dynamics simulations and Boltzmann transport equations [13]. Molecular dynamics simulations can be used to calculate the thermal conductivity of the material. The results from first principle calculations like the density of states and some experimental data serve as inputs to solve the Boltzmann transport equations to get the charge carrier (electron or hole) transport properties of the material like Seebeck coefficient and electrical conductivity.

The electron and phonon transport in bismuth telluride were predicted using first principles and molecular dynamics simulations by Huang et al. [13]. The lattice thermal conductivity of Bi_2Te_3 was calculated by developing suitable interatomic potentials for Bi_2Te_3. The lower limit for thermal conductivity of bismuth telluride was calculated to be 0.2 W/mK at 300 K by considering the effects of short range acoustic and optical phonons. The effect long range phonons on lattice thermal conductivity are neglected because they would be scattered by nanostructure engineering. The electronic transport in the material was calculated using Boltzmann Transport Equations (BTE) with energy dependent relaxation time models and non-parabolic Kane energy dispersion. The temperature dependence of Seebeck coefficient, electrical

conductivity, and electronic thermal conductivity were estimated over a temperature range from 100 to 500 K. It was also found that polar scattering by optical phonons and deformation potential of acoustic and optical phonons dominate the charge carrier transport in Bi_2Te_3. The effect of vacancies on scattering of charge carriers was found to be negligible. It was also found that the temperature dependence of energy bandgap is critical in determining the transport properties of the material in the given temperature regime [13].

The temperature and doping dependence of thermopower of PbTe was studied using Boltzmann Transport Equations by Singh et al. [14]. The transport calculations were performed using Boltzmann transport theory with a constant scattering time approximation. This approximation holds well in the case of degenerately doped semiconductors because the variations of scattering time with energy are less sensitive on the scale of k_BT. The temperature and doping dependence of thermopower calculated using the first principles calculations [14] and Boltzmann transport theory seem to have a good agreement with the experimental values of thermopower determined from samples prepared by Harman et al. [15].

The thermodynamic properties of lead chalcogenides were studied by Zhang et al. [16]. The thermoelectric properties of the materials are closely related to the lattice dynamics and thermodynamic properties. Electronic and lattice dynamic properties of PbTe, PbSe and PbS were studied using DFT calculations [16]. Free energy, vibrational entropy, and heat capacity of the materials were determined based on the results from DFT calculations and compared with the experimental values from the work of Parkinson et al. [17]. The lattice thermal conductivity of the materials was calculated using $Grüneisen$ parameters which could be used to explain the anharmonicity in the lead chalcogenides. Moreover, it was found that effect of spin orbit

interaction had a greater impact on the electronic properties and negligible impact in determining the thermodynamic properties of these materials [16].

The variation of thermoelectric behavior based on the defects present in the material was studied by Mahanti et al. [18] in $AgSbPb_{2n-2}Te_n$. The electronic properties of semiconductors are dominated by defects. Ab initio electronic structure calculations of Ag and Sb substitutional defects in PbTe were carried out, and it was found that these defects affect the density of states near the energy gap. The changes in the electronic structure at the band edges are sensitive to the micro structural arrangements of these defects. The increase in density of states near the energy gap of $AgSbPb_{2n-2}Te_{2n}$ modifies the transport properties of the system and depends on the microstructural ordering arrangements of Ag–Sb pairs in PbTe.

2.10 References

1. K.M. Blundell, Concepts in Thermal Physics. Oxford University Press, USA (2006).
2. E.S. Bozin, C.D. Malliakas, P. Souvatzis, T. Proffen, N.A. Spaldin, M.G. Kanatzidis, S.J.L. Bilinge, Entropically stabilized local dipole formation in lead chalcogenides. *Science* **330**, 1660 (2010).
3. G.J. Snyder, E.S. Toberer, Complex Thermoelectric Materials. *Nature Materials* **7**, 105 – 114 (2008).
4. B. Poudel, Q. Hao, Y. Ma, Y.C. Lan, A. Minnich, B. Yu, X.A. Yan, D.Z. Wang, A. Muto, D. Vashaee, X.Y. Chen, J.M. Liu, M.S. Dresselhaus, G. Chen, Z.F. Ren, High-thermoelectric performance of nanostructured bismuth antimony telluride bulk alloys. *Science* **320**, 634 – 638 (2008).
5. G. Chen, M.S. Dresselhaus, G. Dresselhaus, J.P. Fleurial, T. Caillat, Recent developments in thermoelectric materials. *International Material Reviews* **48**, 45 – 66 (2003).
6. K. Ahn, M.K. Han, J.Q. He, J. Androulakis, S. Ballikaya, C. Uher, V.P. Dravid, M.G. Kanatzidis, Exploring Resonance Levels and Nanostructuring in the PbTe – CdTe System and Enhancement of the Thermoelectric Figure of Merit. *Journal of the American Chemical Society* **132**, 5227 (2010).
7. J. He, N.S. Girard, M.G. Kanatzidis, V.P. Dravid, Microstructure lattice thermal conductivity correlation in nanostructured $PbTe_{0.7}S_{0.3}$ thermoelectric materials. *Adv. Funct. Mater*. **20**, 764 – 772 (2010).
8. M.G. Kanatzidis, Nanostructured thermoelectric: the new paradigm? *Chem Mater* **22,** 648 – 659 (2010).
9. J.P. Heremans, V. Jovovic, E.S. Toberer, A. Saramat, K. Kurosaki, A. Charoenphakdee, S. Yamanaka, G.J. Snyder, Enhancement of Thermoelectric efficiency in PbTe by distortion of the electronic density of states. *Science* **321**, 554 – 557 (2008).
10. Y. Pei, X. Shi, A. LaLonde, H. Wang, L. Chen, G.J. Snyder, Convergence of electronic bands for high performance bulk thermoelectrics. *Nature* **473**, 66 – 69 (2011).

11. K. Biswas, J.Q. He, Q.C. Zhang, G.Y. Wang, C. Uher, V.P. Dravid, M.G. Kanatzidis, Strained endotaxial nanostructures with high thermoelectric figure of merit. *Nature Chemistry* **3**, 160 – 166 (2011).
12. K. Biswas, J. He, I.D. Blum, C.I. Wu, T.P. Hogan, D.N. Seidman, V.P. Dravid, M.G. Kanatzidis, High – performance bulk thermoelectric with all – scale hierarchical architectures. *Nature* **489**, 414 – 418 (2012).
13. B.L. Huang, M. Kaviany, Ab initio and molecular dynamics predictions for electron and phonon transport in bismuth telluride. *Physical Review B* **77**, 125209 (2008).
14. D.J. Singh, Doping–dependent thermopower of PbTe from Boltzmann transport calculations. *Physical Review B* **81**, 195217 (2010).
15. T.C. Harman, D.L. Spears, M.J. Manfra, High thermoelectric figures of merit in PbTe quantum wells. *Journal of Electronic materials* **25**, 1121 – 1127 (1996).
16. Y. Zhang, X. Ke, C. Chen, J. Yang, P.R.C. Kent, Thermodynamic properties of PbTe, PbSe and PbS: First – principles study. *Physical Review B* **80**, 024304 (2009).
17. D.H. Parkinson, J.E. Quarrington, The molar heats of lead sulphide, selenide and telluride in the temperature range 20 °K to 260 °K. *Proc. Phys. Soc., London Sect.A* **67**, 569 (1954).
18. S.D. Mahanti, D. Bilc, Electronic structure of defects and defect clusters in narrow band gap semiconductor PbTe. *J.Phys: Condens. Matter* **16** S5277 – S5288 (2004).

3 Bandstructure in solids and DFT

This chapter briefly outlines band theory in solids and the different models currently used to determine the properties of the material. This chapter also explains the mathematical methods that are used in determining the electronic band structure of semiconductor materials. This Master's research work is based on first principles Density Functional Theory (DFT) calculations and a brief description of DFT is presented. The terminologies and approximations involved are also explained.

3.1 Drude's free electron classical model

Drude [1] proposed the classical free electron model for a metal. Drude's model assumes that atoms in the metal that occupy the lattice sites liberate the valence electrons and form the ionic cores in the crystal. The liberated electrons behave like molecules of classical ideal gas. These free electrons are confined within the solid and hence they are localized within the extent of the solid. This model correctly predicts the properties of metals, which are good thermal and electrical conductors. This model also explains the Wiedemann – Franz law in metals [2].

The main drawback of Drude's model is that it does not describe how the energy is present inside the system. The distribution of electrons in the material is given by Maxwell–Boltzmann statistics with the assumption that electrons are bosons. To reproduce the properties of the actual system, electrons should be considered as quantum particles that follow Pauli's exclusion principle instead of classical particles [3].

3.2 Drude – Sommerfeld model

This model is also a free electron model similar to Drude's model, but it is based on quantum mechanical and thermodynamic principles, applying Pauli's exclusion principle and the behavior of electrons (fermions) is subjected to Fermi – Dirac statistics. The potential inside the metal is assumed constant. Fermi – Dirac statistics describes the distribution of a collection of fermions across energy levels for a system in thermal equilibrium. The expression is given as follows:

$$f(E) = \frac{1}{e^{(E-E_F)/k_B T} + 1}$$

From the Fermi–Dirac distribution, the information regarding the number of states available to be occupied by electrons at a given energy level is not known. This results in defining the concept of density of states $g(E)$ per energy interval dE in volume V of the material which then gives an expression for the number of states that are available for occupancy in a given energy interval, namely,

$$g(E)\,dE = \frac{V}{2\pi^2}\left(\frac{2m^*}{\hbar^2}\right)^{3/2} E^{1/2}\,dE$$

At absolute zero, the electrons in a metal will fill up the possible states two at a time starting from the lowest so that the total energy of the system is kept as low as possible [4]. The highest filled energy level is then known as Fermi energy E_F and the surface in k-space (reciprocal space where the reciprocal lattice of the material is represented) that corresponds to the Fermi energy is called Fermi surface, i.e.

$$E_F = \frac{\hbar^2}{2m^*}(3\pi^2 n)^{3/2}$$

The above equation is the expression for the Fermi energy in terms of carrier density and effective mass of the carrier [4].

The density of occupied states $N(E)$ is given by the product of density of states $g(E)$ and the Fermi – Dirac distribution $f(E)$ which is illustrated in Fig. 3.1 [5].

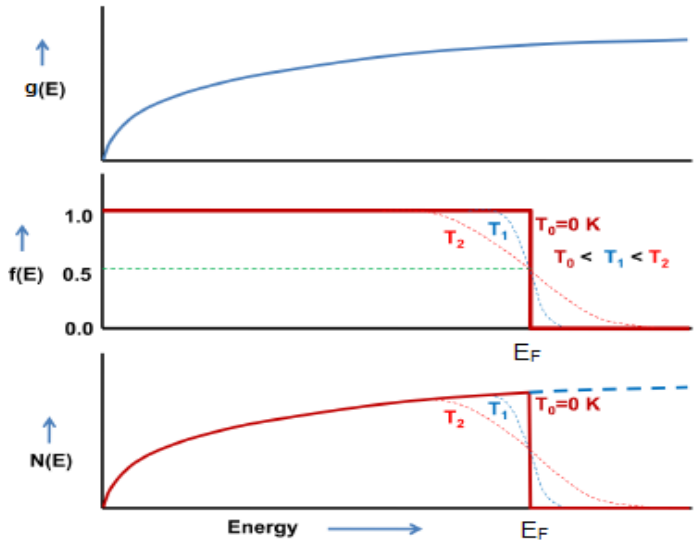

Figure 3.1: Plots of density of states, probability of occupancy, and density of occupied states at different temperatures.

The main difference between the Drude and Drude – Sommerfeld models is that in the former all electrons can gain energy as the temperature increases but in the latter only electrons close to the Fermi energy can gain energy with the rise in temperature. Though the Drude-Sommerfeld model is good, it does not include the variations in the potential experienced by electrons. So this model cannot address anisotropy and the directional dependence of material properties.

Based on the variation of potential with position of ionic cores, electrons are defined as:

1. Truly free electrons – electrons that are very far from the solid, which experiences zero potential. Such electrons completely escape from the solid and are called truly free electrons.
2. Nearly free electrons – electrons that get closer to the solid, experience a slight drop in potential due to their interaction with the overall solid. These electrons are confined to

the solid, but not attached to any of the ionic cores. These are nearly free electrons that take part in the electronic conductivity processes.

3. Bound electrons – electrons that are close to the ionic cores experience a very sharp drop in potential. These are bound electrons that do not participate in the electronic conductivity and are trapped in the corresponding potential wells of the ionic cores.

The properties of the material could be explained based on the quantum mechanical description of electrons and the existence of wave particle duality. The energy of the electron is related to the wave vector k and is expressed as,

$$E = \frac{\hbar^2 k^2}{2m^*}$$

where k is the wave vector, $\hbar$ is the modified Planck constant and m^* is the effective mass of the charge carrier. Travelling electrons that are interacting with different potentials in the crystal lattice have an effective mass (m^*) that is given by the following expression,

$$m^* = \frac{\hbar^2}{d^2E/dk^2}$$

Effective mass accounts for the complex interactions between electrons and the lattice. From the E – k curve, we find that the band effective mass is inversely proportional to curvature.

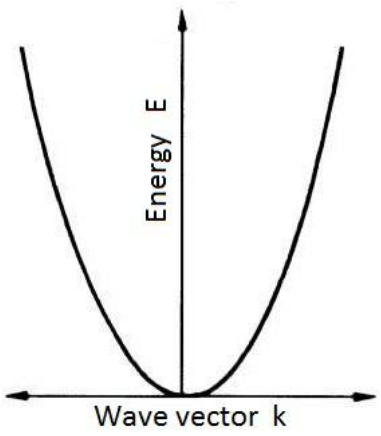

Figure 3.2: E vs. k curve for a free electron

The E vs. k relationship is the same for free, nearly free and bound electrons except that it is continuous for free electrons. In the case of nearly free and bound electrons, the confinement of electrons results in specific permitted k values that lead to specific values of energy [5].

To understand the E vs. k relationship and the presence of band gaps in a material, one needs to understand the Wigner–Seitz cell and Brillouin zone. A Wigner–Seitz cell about a lattice point is the region in space that is closer to that lattice point than to any other lattice point, and the first Brillouin zone (BZ) is defined as the Wigner–Seitz primitive cell about a lattice point in reciprocal space [3]. Nearly free electrons moving in a material with a periodic structure displays wave like behavior. Whenever a wave vector touches the BZ boundary that is associated with the periodic nature, diffraction occurs. The diffraction causes the E vs. k relationship to distort near the Bragg planes (BZ boundaries). This distortion causes some of the energy levels to become forbidden for the electrons, which results in the presence of band gaps in materials and is represented in the extended zone scheme as well as the flat band diagram of Fig. 3.3 [5].

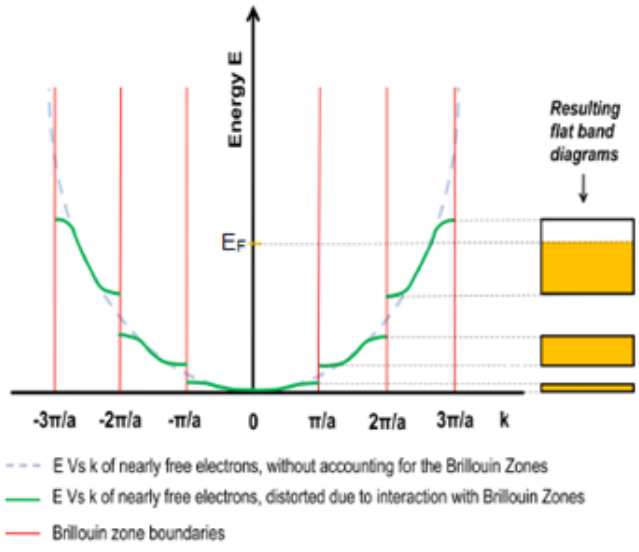

Figure 3.3: The extended zone representation of the E-k relationship and equivalent flat band diagram.

All the above analysis is based on the free electron approximation, i.e. an already existing solid is considered that has fixed ionic cores at the lattice points and electrons are free to move through the solid.

3.3 Tight binding model

In the case of the tight binding model, the solid does not already exist. The solid is built by bringing the individual atoms closer. All the electrons are bound to their corresponding atoms initially when they are far apart from each other. As the atoms are brought close to each other to build a solid, the outer shell electrons begin to overlap and the energy level of these outer shell electrons are forced to split without violating Pauli's exclusion principle as shown in Fig. 3.4 [5]. In the tight–binding model, the interatomic distance plays a very important role in determining the band structure [3].

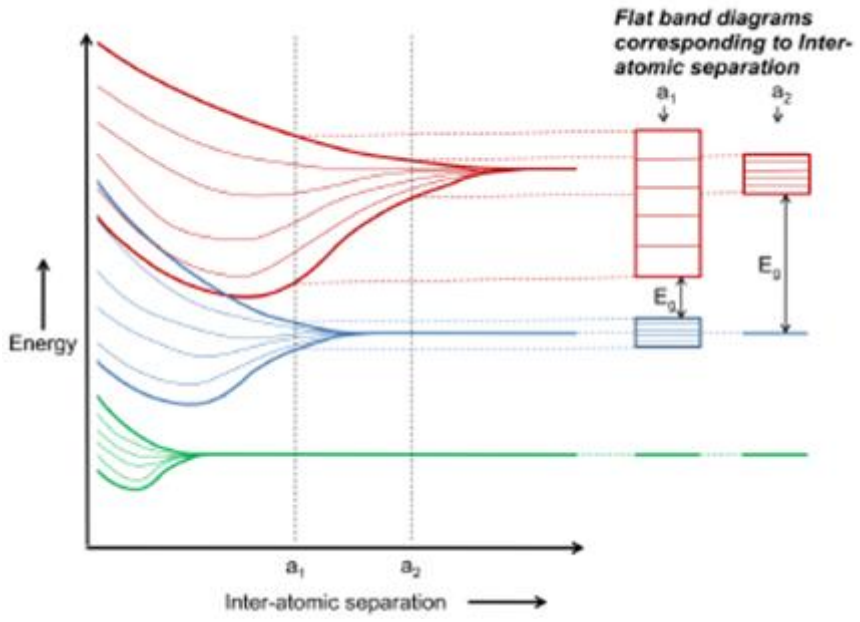

Figure 3.4: A schematic representation of tight binding model at two different inter-atomic separations.

Corresponding to the equilibrium position, the material displays a specific band structure. Based on this theory, the application of pressure to the material changes its band structure and also its

properties. At sufficiently high pressure, an insulating material becomes a conducting material because of the change in the band gap E_g.

3.4 Semiconductors

Semiconductors are a class of materials which have a completely filled valence band and an empty conduction band and whose conductivity is much less compared to metals, but the conductivity can be tailored by different techniques. Semiconductors are broadly classified into intrinsic and extrinsic semiconductors.

Intrinsic semiconductors are pure and have no dopants (impurities) added to them. The conductivity is a function of temperature only. For each electron in the conduction band, there is a hole in the valence band. Both bands support the conduction process. In this case, $n = p = n_i$, the carrier concentration. The expression for electrical conductivity is,

$$\sigma = n_i e(\mu_e + \mu_h)$$

Extrinsic semiconductors are further classified into p–type and n–type semiconductors. Doping a IV A element with a V A element results in a n–type semiconductor and doping a IV A element with a III A element results in a p–type [5]. The expressions for conductivity of p–type and n–type semiconductors are as follows:

$$\sigma = pe\mu_h; \sigma = ne\mu_e$$

Dopants dominate the semiconductor behavior because they shift the Fermi energy of the material based on the doping level. The Fermi energies in different types of semiconductors are shown in Fig. 3.5.

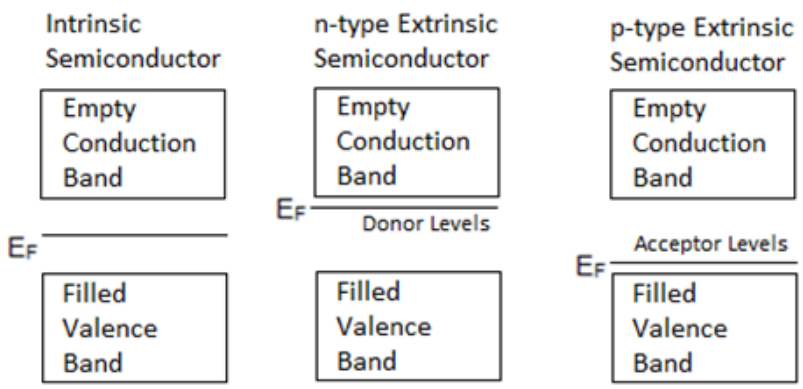

Figure 3.5: Position of the Fermi energy level in different types of semiconductors.

The position of the Fermi energy level in semiconductors is very important because when two semiconductors are brought in physical contact, the value of the Fermi energies determine the direction in which the electrons flow to equalize the Fermi energies. In the case of semiconductors, both charge carrier concentration and mobility are affected by temperature. The carrier concentration increases with temperature, but the charge carrier mobility decreases as the temperature increases because there is an increased probability of charge scattering due to carrier interactions with phonons. The reduction in charge mobility is less when compared to the increase in carrier concentration; and as a result, the conductivity of semiconductors increases with increase in temperature.

Based on the bandgap of materials, semiconductors are classified as direct and indirect bandgap semiconductors. In the case of direct bandgap semiconductors, the highest occupied level (valence band maximum) and the lowest unoccupied level (conduction band minimum) are in the same location in k–space. For an electron to go to the conduction band, it has to absorb only the right amount of energy required for the transition. This is not the case for indirect bandgap materials whose conduction band minimum and valence band maximum at different locations in k–space as shown in Fig. 3.6.

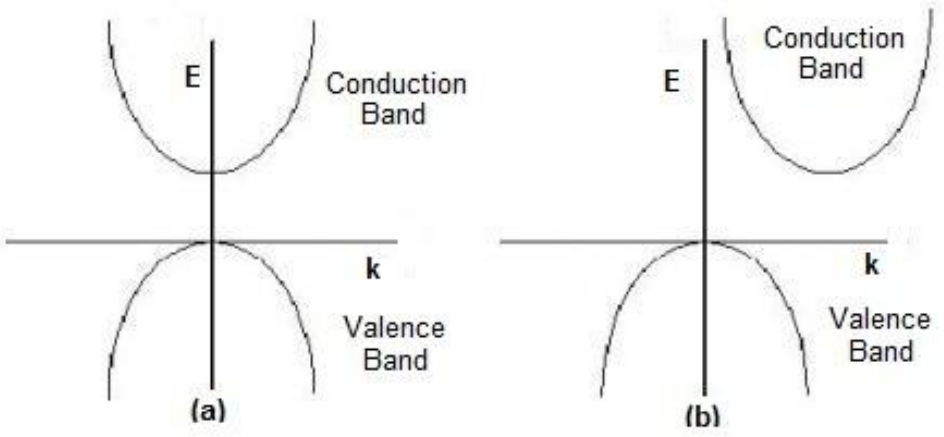

Figure 3.6: Types of semiconductors (a) Direct bandgap semiconductor (a) Indirect bandgap semiconductor.

For an electron to make a transition in indirect bandgap materials, it not only needs to absorb the appropriate energy, but also encounter an appropriate lattice vibration (phonon) to transport it to the other location in k–space. The coupling of the probabilities of an electron absorbing the right amount of energy and encountering a phonon makes the overall probability of the transition of an electron in an indirect bandgap material relatively low. For this reason, direct bandgap semiconductor materials like gallium arsenide are preferred over indirect bandgap materials like silicon for making optical devices like LEDs and semiconductor LASERs [1].

3.5 Density Functional Theory–Introduction

The electronic structure calculations are widely used in a variety of applications like geometry optimization, calculation of excitation energy and reaction on surfaces. Computational studies help people understand experimental results and study systems that are too expensive and difficult to model experimentally. Electronic structure computations are based on the stationary or time-independent Schrödinger equation and solving it requires numerical methods to get the required information about the system from the wave functions. In quantum mechanics, the analogue to Newton's law is the Schrödinger equation. The quantum state at every instant of

time of a quantum system of N electrons is stored within the wave function $\psi(\vec{r},t)$ which is defined by the Schrödinger equation [6].

For systems with more than two electrons, the time-independent part of the Schrödinger equation represents a many-body problem and cannot be solved analytically. The time independent Schrödinger equation is given by,

$$\hat{H}\psi_i(r) = E_i\psi_i(r)$$

$$\left\{-\frac{\hbar^2\nabla^2}{2m} + V(r)\right\}\psi_i(r) = E_i\psi_i(r)$$

$$\left\{\sum_i^N [-\frac{\hbar^2\nabla^2}{2m} + V(r_i)]\right\}\psi_i(r_1, r_2, \ldots r_N) = E_i\psi_i(r_1, r_2, \ldots r_N)$$

The time-independent Schrödinger equation for a single body system and many-body system (N particles) are represented above. $\hat{H}$ is the Hamiltonian operator (total energy operator), the E_i are the eigenenergies of the system, m is the mass of the particle, $\frac{\hbar^2\nabla^2}{2m}$ is the kinetic energy operator, $V(r)$ is the potential energy operator and $\psi_i(r)$ is the eigenfunctions of the system. The Hamiltonian operator is expressed as,

$$\hat{H} = \hat{\mathrm{T}}_e + \hat{\mathrm{T}}_N + \hat{\mathrm{V}}_{e-e} + \hat{\mathrm{V}}_{N-N} + \hat{\mathrm{V}}_{e-N}$$

where $\hat{\mathrm{T}}_e$ is the operator corresponding to the quantum kinetic energy of the electrons, $\hat{\mathrm{T}}_N$ the operator corresponding to quantum kinetic energy of the nucleus, $\hat{\mathrm{V}}_{e-e}$ the electron-electron repulsion operator, $\hat{\mathrm{V}}_{N-N}$ the electrostatic nucleus-nucleus repulsion operator and $\hat{\mathrm{V}}_{e-N}$ the electrostatic attraction operator between the nucleus and electron.

The motion of the particles is coupled and they do not move independently. This represents a very complex problem that is difficult to solve. To overcome this difficulty, the problem is simplified by making the Born Oppenheimer approximation [7]. Since the motion of the nuclei

is much slower when compared to that of the electrons, the kinetic energy of the nuclei in the Hamiltonian can be ignored and inter- nuclear repulsion becomes constant when solving for the electrons, i.e. the electrons are treated as quantum particles in a field of fixed nuclei.

Variational principle plays a prominent role in all quantum applications. It is a method employed using either the minimum energy or maximum entropy principles to determine the state of a system by identifying the extremum of the functional. In our case, we determine the thermodynamic or stable equilibrium state of the system by finding the minimum energy of the system. It states that the energy computed as the expectation value of the Hamiltonian operator from any trial wave function, will be upper bound to the ground state energy (E_0) of the system.

$$E[\psi] = \frac{\langle \psi | \hat{H} | \psi \rangle}{\langle \psi | \psi \rangle} \; ; E[\psi] \geqslant E_0$$

If $E\,[\psi] = E_0$, then ψ is the ground state wave function and the reverse is also true. Computational requirement to solve the N electron system scales as a factor of N^N to represent the wave function ψ of the system in k space and is beyond computing capabilities. To reduce the computational intensity of these calculations, methods have been proposed using different approximations and assumptions that define the system. A few of the methods that are commonly used are discussed here.

3.6 Hartree method

Hartree developed a self-consistent method, which makes an initial guess of the wave functions of the atomic orbitals in the system and uses it to construct the one-electron Hamiltonian operator. In this independent particle model, the electrons move in an effective potential representing the attraction of the nuclei and the average effect of the repulsive interactions of the electrons [8].

The Hamiltonian operator consists of the kinetic energy of the electrons, the electron–nucleus attraction potential, and an effective potential, the Hartree potential, which approximates the electron–electron repulsion potential. Solving the equation with these inputs provides an updated set of wave functions of the atomic orbitals. The iterative procedure is repeated using this updated set until the convergence criterion is reached. The Hartree equations can be obtained from the variational principle.

The many body wave function is written as a product of single orbitals, namely,

$$\psi(r_1, r_2, \ldots r_n) = \phi_1(r_1)\phi_2(r_2)\ldots\phi_n(r_n)$$

$$\left\{-\frac{\hbar^2\nabla^2}{2m} + \sum_{\mathrm{I}} \mathrm{V}(\mathrm{R_I} - r_i) + \sum_{j\neq i}\int \left|\phi_j(r_j)\right|^2 \frac{1}{\left|r_\mathrm{j} - r_i\right|} dr_\mathrm{j}\right\}\phi_i(r_i) = E_i\phi_i(r_i)$$

The first term in the above equation represents the kinetic energy of the electrons, the second, the electron–nuclei Coulombic attraction potential, and the last, the Hartree potential that contains the Coulombic repulsion between electron i and the average electron charge density. n simultaneous integro-differential equations are solved iteratively for n orbitals. The main drawback of the Hartree model is it does not include electron correlations, which results from the instantaneous interactions between electrons in the system. Since the Hartree potential considers only the repulsion between the electron and the average electron density, it accounts for more electrostatic repulsion than actually exisits, leading to a higher energy than what the system actually sees. Furthermore, the wave functions are not anti-symmetric. According to Pauli's Exclusion Principle, the electronic wave function should be anti-symmetric under the exchange of any two particles in the system [9], i.e.

$$\psi(r_1, r_2, .r_j..r_k..r_N) = -\psi(r_1, r_2, .r_k..r_j..r_N)$$

To include this, Fock extended Hartree's method to Slater determinants. The anti-symmetric wave function is constructed using Slater determinants of individual orbitals. The Slater determinant is an expression in matrix form that describes the wave function of a multi-body system satisfying Pauli's exclusion principle. Hartree–Fock molecular orbitals are the eigenfunctions of the set of one electron Hamiltonians. The determinant vanishes if two states are identical. The Hartree–Fock equations are again obtained from the variational principle. All the wave functions are written as a single Slater determinant [10] such that

$$\psi(r_1, r_2, \ldots r_n) = \frac{1}{\sqrt{n!}} \begin{vmatrix} \phi_\alpha(r_1) \ldots . \phi_\nu(r_1) \\ \ldots . \\ \phi_\alpha(r_n) \ldots . \phi_\nu(r_n) \end{vmatrix}$$

$$\left\{ -\frac{\hbar^2 \nabla^2}{2m} + \sum\nolimits_{\mathrm{I}} \mathrm{V}(\mathrm{R_I} - r_i) + \sum_j \int \left|\phi_j(r_j)\right|^2 \frac{1}{\left|r_\mathrm{j} - r_i\right|} dr_\mathrm{j} \right\} \phi_i(r_i)$$

$$- \left\{ \sum_j \int \phi_j(r_j) \frac{1}{\left|r_\mathrm{j} - r_i\right|} \phi_i(r_j) dr_\mathrm{j} \right\} \phi_j(r_i) = E_i \phi_i(r_i)$$

where n is the number of orbitals. It has all the terms as in Hartree's equation with an additional negative term in the expression that accounts for the anti-symmetric requirement of the wave function. Even though the Hartree-Fock wave functions include the exchange effects, they are not exact because the electron correlation is still neglected.

Density Functional Theory (DFT) is a technique that accounts for the correlation effects which maps the many-body problem with interacting electrons to a single-body problem with the assumption of non-interacting electrons. DFT provides a perfect balance between the computational cost and accuracy [11].

The external potential in the time-independent Schrödinger equation describes the interaction of the electrons with the nucleus or external field. Thus the external potential and the number of

electrons completely define the system. The wave functions $\psi(r)$ are uniquely determined via the time-independent Schrödinger equation and everything is a functional of external potential and the number of electrons.

3.7 Governing principle of DFT

The governing principles of DFT are given by the Hohenberg and Kohn theorems [12]. The Hohenberg–Kohn theorems prove that once the electron–electron interaction is given, the external potential will be given by the ground state electronic density from which the wave function can be found. In DFT, instead of solving the highly coupled time-independent Schrödinger equation for the many-body wave functions, the ground state density is determined. The particle density is the key variable. The complex many-bodied electronic wave function is replaced by the electronic charge density, which overcomes the fundamental limitation of dealing with many electron systems.

The first Hohenberg–Kohn theorem states that the external potential uniquely determines the ground state charge density and the charge density uniquely determines the external potential [12]. The ground state density, thus, determines the number of electrons N, the electron-electron potential of the time independent Schrödinger equation and, thus, the wave functions. The universal density functional is given by

$$F(\rho(r)) = \langle \psi | \hat{T} + \hat{V}_{ee} | \psi \rangle$$

$$\rho(r) = \sum_{i}^{N} |\psi_i(r)|^2$$

The second Hohenberg–Kohn theorem provides the energy variational principle, i.e. the density that minimizes the total energy is the exact ground state density [12]. This results in a new Schrödinger like equation that is expressed in terms of the charge density only, namely,

$$E_v(\rho^\star(r)) = F(\rho^\star(r)) + \int \hat{V}_{ext}(r)\rho^\star(r)\,dr \geqslant E_0$$

$\rho^\star(r)$ determines the ground state wave function, that can be taken as the trial wave function in the above external potential, i.e.

$$\langle \psi^* | \hat{H} | \psi^* \rangle = \langle \psi^* | \hat{V}_{ext} + \hat{T} + \hat{V}_{ee} | \psi^* \rangle = F(\rho^\star(r)) + \int \hat{V}_{ext}(r)\rho^\star(r)\,dr$$

Kohn and Sham proposed to replace the system of interacting electrons with a system of non-interacting electrons which is easier to evaluate. The Kohn–Sham formalism of DFT is popular in solid state physics and it scales favorably with system size when compared to the Hartree–Fock (HF). DFT is quite successful in describing interacting systems, isolated molecules, and solid state systems and is well-suited for modern parallel computing techniques.

The electrons in the Kohn–Sham system are Kohn–Sham electrons that do not interact and are in an external potential (Kohn–Sham potential) such that their ground–state charge density is identical to the charge density of the interacting system. For this system of non–interacting electrons, the Slater determinant is exact and the kinetic energy is well-defined. The resulting density represents the density of the real system of interacting electrons. Minimizing the total energy functional leads to Schrödinger-like equations with an effective potential known as the Kohn–Sham equations that provide an approximation to the density functional for the real systems under consideration. Thus,

$$[-\frac{\hbar^2\nabla^2}{2m} + \upsilon_H(r) + \upsilon_{xc}(r) + \upsilon_{ext}(r)]\psi_i(r) = \hat{H}_{KS}\psi_i(r) = E_i\psi_i(r)$$

$$\upsilon_H(r) = \int \frac{\rho(r^\star)}{|r - r^\star|} dr^\star;\ \ \upsilon_{xc}(r) = \frac{\delta E_{xc}[\rho(r)]}{\delta\rho(r)}$$

The electronic Hamiltonian operator consists of a non–interacting kinetic energy operator and KS potential contributions. The KS potential is made up of the Hartree potential $\upsilon_H(r)$, external potential $\upsilon_{ext}(r)$, and the exchange correlation potential $\upsilon_{xc}(r)$. The external potential is the

same as that for the real interacting system, which is the attraction between the nuclei and electrons and any other external field that might be present in the system. The exchange correlation term consists of all the unaccounted for contributions like electron–electron interactions and the difference in kinetic energies between the non – interacting and interacting systems [13]. Therefore, the KS universal density functional $F[\rho(r)]$ is written as

$$F[\rho(r)] = T_S[\rho(r)] + E_H[\rho(r)] + E_{xc}[\rho(r)]; \quad E_H[\rho(r)] = \frac{1}{2}\int\int \frac{\rho(r)\rho(r^\star)}{|r - r^\star|}\, dr^\star\, dr$$

The KS–DFT formalization is similar to mean–field theory with a self consistent effective one–electron Schrödinger equation for KS orbitals, but it also includes all the correlation effects on the ground state electronic density and the total energy of the system. If the exact value of the exchange correlation potential is known, then solving these KS equations is equivalent to solving the exact time-independent Schrödinger equation with the Born–Oppenheimer approximation [14]. Unfortunately determining the exact value for $E_{xc}[\rho(r)]$ is very complex and hence, approximations to get the exchange–correlation functional are needed.

3.8 Exchange correlation functional

The total energy functional has a term that includes all the effects of exchange and correlation, which depends on the density over all the space. The Local Density Approximation (LDA) treats homogenous systems like metals and semiconductors with good accuracy. In LDA $E_{xc}[\rho]$ are defined as

$$E_{xc}^{LDA}[\rho] = \int \rho(r)\epsilon_{xc}^{LDA}(\rho)\, dr$$

$E_{xc}^{LDA}[\rho]$ is the exchange and correlation energy density of a uniform electron gas of density $\rho(r)$ [15]. The accuracy of predictions for bond energies, lattice parameters, and other molecular properties using LDA are moderate. In this approximation, the exchange–correlation potential

only depends on the density at the point where the functional is evaluated and contains no information about the neighboring points.

Semi-local functionals are an improvement over the local approximations. They not only depend on the density at that point, but also on the gradient of density. In the case of electrons in a rapidly changing external potential, semi-local functionals give a better approximation, and one such functional is the Generalized Gradient Approximation (GGA). It is used for inhomogeneous systems and uses the local charge density at a given point including the gradient of charge density when approximating the exchange correlation energy [15]. It explicitly incorporates the density gradient dependence into $E_{xc}[\rho]$ and is quite successful in fixing the over-binding nature of LDA. The expression for $E_{xc}^{GGA}[\rho]$ is thus rewritten to include the reduced density gradient, i.e.

$$E_{xc}^{GGA}[\rho] = \int \rho(r)\epsilon_{xc}^{GGA}(\rho, \nabla\rho)\, dr$$

An application of DFT requires the Kohn–Sham equations to be solved numerically by representing the electronic wave functions as a linear combination of a basis set. The basis set provides a good physical description of the system and is used to create the orbitals, which are expanded as a linear combination of the basis functions. A basis set composed of a set of plane waves with a cutoff wavelength is most commonly used in calculations involving systems with periodic boundary conditions. To further reduce the computational intensity, pseudo-potentials are used that assume the electrons in the inner atomic shells are tightly bound to the nucleus of the atom and are not affected by external perturbations.

The tightly bound core electrons are chemically inactive and make negligible contributions to properties like the bond energy, etc. The core states are localized near the nucleus, leading to oscillations of the valence wave functions irrespective of the basis set used. A large number of

basis functions is needed to capture these oscillations. This is overcome by the pseudo-potential approximation where the all electron potential is replaced by an effective potential [16].

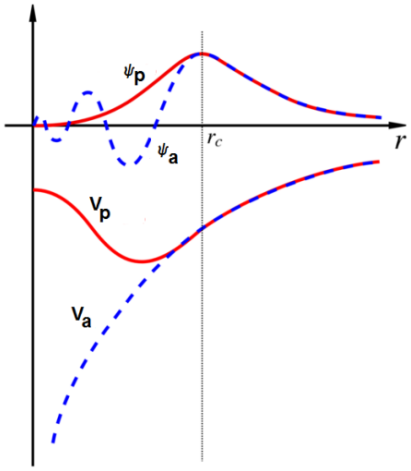

Figure 3.7: Representation of pseudo-potential and pseudo wave function.

In Fig. 3.7 [17], V_a is the actual Columbic potential for core electrons and V_p is the effective potential term that is used in DFT calculations. After the chosen cutoff radius r_c, both the pseudo and actual functions are the same. Pseudo-potentials with a larger cutoff are softer, and the convergence in this case is fast.

The initial guess for the charge density is used to calculate the effective potential; and once the effective potential is calculated, the electron density is recalculated and tested using criteria for convergence. The above process is repeated until the convergence criterion is satisfied. The schematic representation of the self-consistent calculation is represented in the flowchart as in Fig. 3.8.

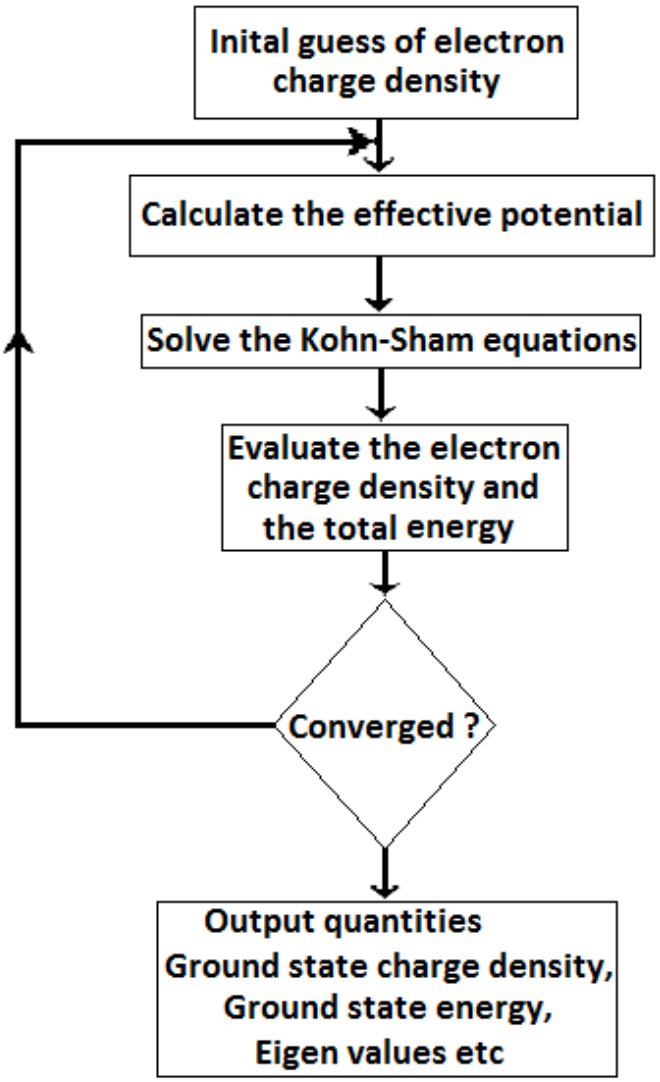

Figure 3.8: Flowchart representing the self-consistent procedure for solving Kohn-Sham equations.

3.9 References

1. P. Drude, Zur Elektronentheorie der metalle. *Annalen der Physik* **303**, 566 (1900).
2. S.A. Holgate, Understanding Solid State Physics. CRC Press, Boca Raton (2010).
3. P. Hofmann, Solid State Physics. WILEY–VCH, Weinheim (2008).
4. N.W. Ashcroft, N.D. Mermin, Solid State Physics. Harcourt College Publishers, Orlando (1976).
5. http://nptel.iitm.ac.in/courses/113106040/
6. K. Capelle, A Bird's–Eye view of Density–Functional theory. *Brazilian Journal of Physics* **36(4A),** 1318 – 1343 (2006).
7. M. Born, R. Oppenheimer, Zur Quantentheorie der Molekeln. *Annalen der Physik* **389**, 457 – 484 (1927).
8. D.R. Hartree, *Proc. Cambridge Phil. Soc*. **24**, 89, 111, 426 (1928).
9. A. Szabo, N.S. Ostlund, Modern Quantum Chemistry, Macmillan, New York (1982).
10. R. Krishnan, M.J. Frisch, J.A. Pople, Contribution of triple substitutions to the electron correlation energy in fourth order perturbation. *J. Chem. Phys* **72**, 4244 (1980).
11. P. Hohenberg, W. Kohn, Inhomogeneous Electron Gas. *Phys. Rev*. **136**, B864, (1964).
12. W. Kohn, L.J. Sham, Self – Consistent equations including Exchange and Correlation Effects. *Phys. Rev*. **140**, A1133 – A1138 (1965).
13. http://ocw.mit.edu/courses/materials-science-and-engineering/3-320-atomistic-computer-modeling-of-materials-sma-5107-spring-2005/video-lectures/
14. D. Marx, J. Hutter, Ab initio molecular dynamics: Theory and implementation. In Modern methods and algorithms of quantum chemistry. **1**, 301 (2000).
15. W. Kohn, Nobel Lecture: Electronic Structure of Matter – wave functions and density functional. *Rev. Mod. Phys.* **71**, 5 (1999).
16. W.E. Pickett, Pseudo-potential methods in condensed matter applications. *Computer Physics reports* **9** (3), 115 – 197 (1989).
17. http://en.wikipedia.org/wiki/File:Sketch_Pseudo-potentials.png

4 Temperature effects on the electronic properties of PbTe

The chapter primarily focuses on determining the linear temperature dependence of the direct energy bandgap of the material and also outlines the procedure to calculate the conductivity effective masses of charge carriers and the total density of states effective masses from the results obtained from first principles DFT calculations.

4.1 Non-parabolic energy bands in semiconductors

PbTe is a well-known thermoelectric material in the 450–850 K temperature range. It has a rock salt (NaCl) structure as shown in Fig. 4.1.

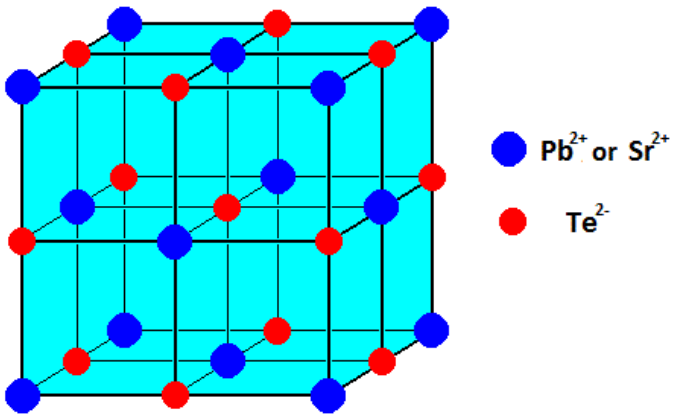

Figure 4.1: Crystal Structure of PbTe

PbTe is a narrow direct bandgap semiconductor. A wide range of energy bandgaps are found in the literature ranging from 0.09 to 0.19 eV [1]. Through our first principles DFT calculations, we get the energy bandgap to be 0.13 eV at 0 K. Generally, the energy bandgap in materials estimated by DFT calculations are underestimated because of the discontinuity in the exchange-correlation energy.

The density of states with the energy bandgap of the material is compared in Fig. 4.2 [1]. Density of states describes the number of energy states available for electron occupancy at each energy level. Higher density of states at a given energy level implies many energy states are available for electron occupation and similarly zero density of states means that no energy states are available for electron occupation. These regions are termed as energy bandgaps.

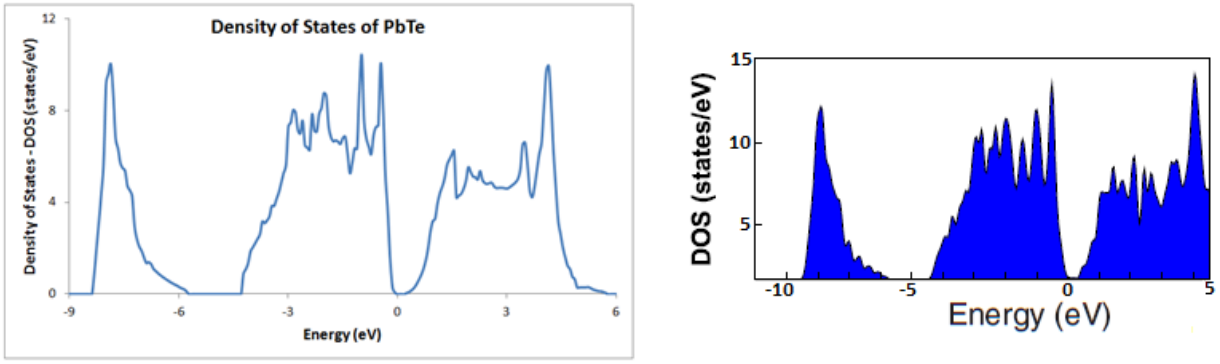

Figure 4.2: Comparison of density of states (DOS) of PbTe at 0 K

The peculiar properties of the material such as, low lattice thermal conductivity at elevated temperatures, strong temperature dependence of carrier scattering, and increase in energy bandgap with increasing temperature attracted interest in understanding the physics of its phase transitions, transport properties, and electronic energy bandgap. The general assumption of parabolic energy bands does not hold for lead telluride. PbTe has a complex band structure, and the non–parabolicity of the conduction and valence bands have to be considered to accurately determine the electronic properties of the material [2].

In the case of narrow bandgap semiconductors, at high applied fields and temperatures, the carriers gain enough energy; they are excited to the conduction band resulting in band interactions which leads to a complex band structure [3]. The band structure of PbTe showing only the conduction and valence band is represented in Fig. 4.3. The valence band maximum and the conduction band minimum (band edges) are located at the same point (L) in the Brillouin

zone implying that the material is a direct bandgap semiconductor. Direct bandgap semiconductor materials are generally preferred because carriers require only the right amount of energy to get excited to higher energy levels. Indirect bandgap semiconductors, on the other hand, require the right amount of energy and must interact with phonons to have a momentum change. The curvatures at the band edges play a very important role in determining the mobility of charge carriers. The rate of change of slope of the band structure provides a very important parameter called the effective mass that is used in determining various transport properties of the material.

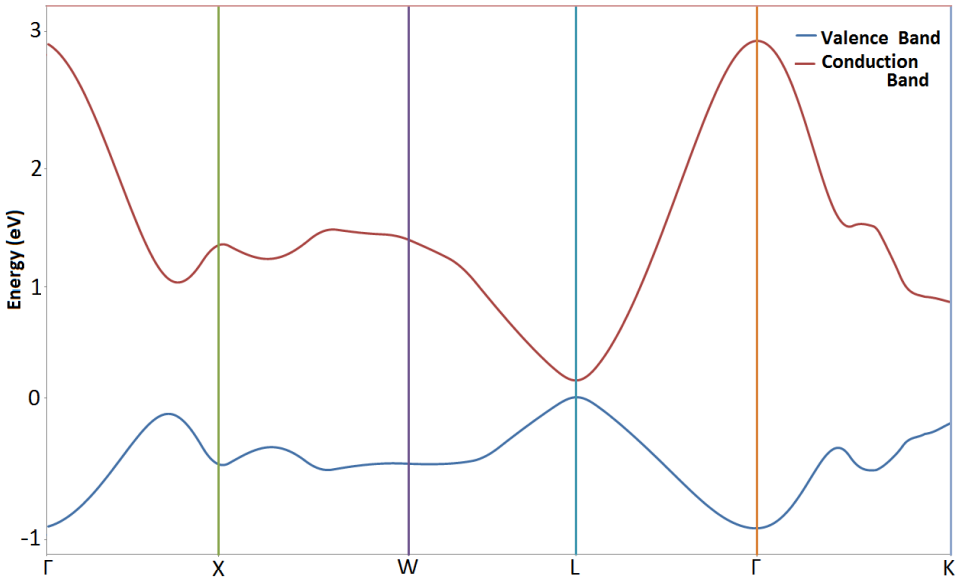

Figure 4.3: Band structure of PbTe at 0 K.

In the case of narrow bandgap semiconductors, the non–parabolic Kane two-band model [4] for the energy dispersion is used, which gives a good approximation for the density of states at the conduction and valence band edges. The dispersion relation of the bands is of the form [5]

$$E\left(1+\frac{E}{E_g}\right)=\frac{\hbar^2 k^2}{2\,m^*}$$

where E is the energy from the band edge, E_g is the bandgap, k is the wave vector and m^* is the effective mass of the carrier. The Kane two-band model assumes that the band extrema for the conduction and valence band occurs at the same k-point [5], which is the case in PbTe (valence band maximum and conduction band minimum occurs at point L $(1/2, 1/2, 1/2)$ of the first Brillouin zone) as shown in Fig. 4.3.

4.2 Temperature effects on the crystal structure of PbTe

The properties of the system vary with changes in temperature of the material. The temperature effect is one of the primary reasons for the differences in electronic properties of the material like energy bandgap and effective mass of the charge carriers which in turn have a significant impact on transport properties such as, the Seebeck coefficient and electrical conductivity of the material. Hence, at finite system temperatures, the band energies of the material differ from the energy values obtained at zero temperature [6]. The overall expansion of the crystal due to thermal effects causes the deviation from frozen lattice approximation at zero temperature [7].

The first principles study on the lattice dynamics and thermodynamic properties of PbTe by Zhang et al. [1] gives the lattice parameters of the material at different temperatures. The unit cell was expanded and compressed to a set of constant volumes by relaxing the atoms and cell shape. The equilibrium volume at a given temperature was obtained by minimizing the free energy. Then the equilibrium lattice parameters at different temperatures were obtained by fitting the free energy curve vs. lattice parameter with third-order Birch-Murnaghan equation of state. We use these lattice parameters at different temperatures in our first principles DFT calculations. Moreover, it was observed by Simon et al. [8] that the thermal effects cause Pb^{2+} ionic cores to displace from their equilibrium lattice positions. We also incorporate these structural changes along with the lattice thermal expansion in our study.

At elevated temperatures, the displacement of Pb atoms is significantly larger than the Te atoms in the rock salt structure [7]. This phenomenon was observed by studying the measured Bragg X–ray diffraction peaks from the material in the specified temperature range. It was believed that the attenuation in Bragg diffraction peaks might be because of Debye–Waller effects (a phenomenon that describes the attenuation of X–ray or neutron scattering due to thermal motion).

Recently Simon et al. [8] experimentally observed that lead chalcogenides formed structurally fluctuating dipoles from the undistorted ground state on heating. Based on the neutron powder diffraction data, a significant attenuation in the Bragg peaks was observed and the extent of loss in intensity was large. The atomic pair distribution function (PDF) analysis was also preformed to confirm the characteristic structural property of the material and it was found that quasistatic structural dipoles were formed. It was also believed that the off centering of Pb^{2+} ions (atomic displacements) had a trend and it was more likely in the <100> direction. In the high temperature region, the temperature dependence of lattice parameter and the above mentioned atomic displacement parameter were linear.

The refined distortion saturated at a maximum value of 0.24 Å, and there was no change in crystal symmetry at approximately 450 K. It was believed that these structural effects could explain the enhanced bandgap for the locally distorted structure indicating the increase in bandgap with increase in temperature [8].

Experimental studies on electronic properties of PbTe revealed that PbTe has a linear increase in the direct bandgap till 400 K and then it saturates and the effective masses of charge carriers linearly increase with temperature.

4.3 Methodology

In this work, we tried to capture this temperature dependence of bandgap and effective masses using the unique structural characteristics of lead chalcogenides at elevated temperatures. The structural and electronic property calculations were performed by first principles density functional theory using the VASP (Vienna ab initio simulation package) [9, 10] program together with projector – augmented wave (PAW) potentials [11]. All the calculations were done using the generalized gradient approximation (GGA) developed by Perdew and Wang [12] for the exchange and correlation potential. The 12X12X12 Monkhorst Pack [13] k–point mesh together with a Methfessel–Paxton [14] smearing of 0.1 eV was employed for the Brillouin zone integration. An energy cut off of 400 eV was used in the plane wave expansion. The spin orbit interaction was also included in the system.

Incorporating the effects of temperature on the lattice parameter and the displacement of Pb^{2+} ionic cores, we relax the system to get the stable configuration. The lattice constants a(T) from DFT calculations [1] and the displacement of Pb^{2+} ionic cores at different temperatures till 400 K deduced from experimental observations [8] are as listed in Table 4.1.

Table 4.1: Lattice constant of PbTe and the displacement of Pb^{2+} at different temperatures.

Temperature in K	Lattice constant in Å[1]	Displacement of Pb^{2+} ions in Å[8]
0	6.556	0
100	6.575	0.055
200	6.5905	0.145
300	6.6046	0.18
400	6.6185	0.22

At finite temperatures atoms in the crystal structure vibrate in the phase space (characterized by 3 position coordinates and 3 momentum coordinates). This vibration along with thermal crystal expansion give rise to a phenomenon called vibrational entropy. The vibrational entropy increases with increase in temperature of the system and it affects the energy and thermodynamics of the system under consideration. Though the temperature effects are incorporated in our calculations through the structural changes of the system (lattice thermal expansion and atomic distortions), the vibrational entropy of the system is neglected because the DFT calculations are performed at absolute zero temperatures. The crystal structure with periodic boundary conditions was adopted. At each temperature, the displacements were incremented in steps in all three directions to get the stable configuration of the system. For example at 100 K, the displacement of ions is incremented in steps of 0.011 Å till 0.055 Å in all three directions. The displacement of Pb^{2+} ionic cores from equilibrium position at 300 K is shown in Fig. 4.4.

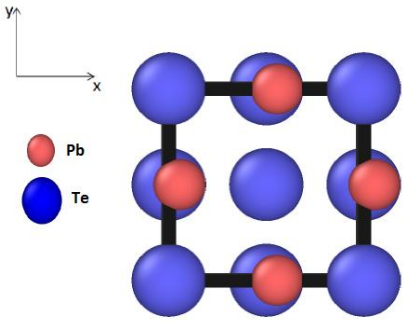

Figure 4.4: Top view of the rock salt structure of PbTe showing displacement of Pb^{2+} ions in <100> at 300 K.

4.4 Energy bandgap vs. Temperature

The energy bandgap of PbTe at different temperatures was found experimentally and was observed that the bandgap linearly increases till 400 K and remains constant above 400 K [15].

The temperature dependence of band gap E_g is given by the following equation as stated by Mahanti et al. [2],

$$E_g(T) = 0.19 + (0.42\text{x}10^{-3})T, T \leq 400K$$

$$E_g = 0.358, T > 400K$$

The experimental data and our results from DFT calculations for the bandgap at different temperatures are compared in Fig. 4.5. The linear temperature dependence of bandgap E_g from our calculation is given by the following expression,

$$E_g(T) = 0.142 + (0.5\text{x}10^{-3})T, T \leq 400K$$

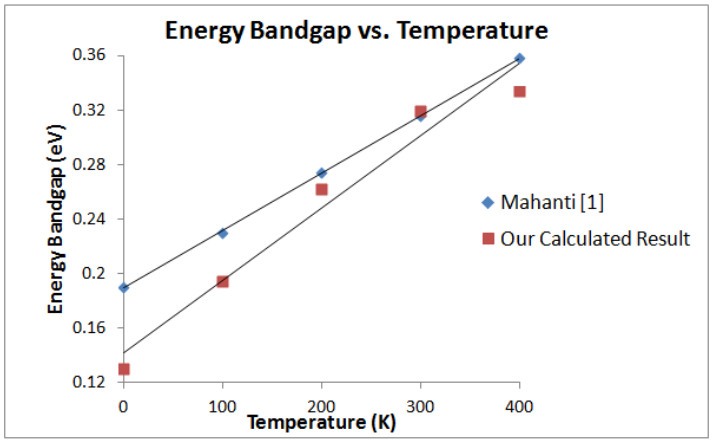

Figure 4.5: Bandgap of PbTe vs. Temperature.

The displacement of atoms from their equilibrium positions after relaxation is listed in Table 4.2 for each temperature along with the energy bandgap. We could now relate the structural distortions due to the temperature effects and the enhanced bandgap of the material. This distortion of Pb^{2+} ionic cores saturates at 450 K and the direct energy bandgap of the material also saturates at approximately 400 K. The Density of States (DOS) from our first principles calculations at different temperatures is shown in Fig. 4.6 and Fig. 4.7 clearly shows the density of states at the band edges and the bandgap at different temperatures.

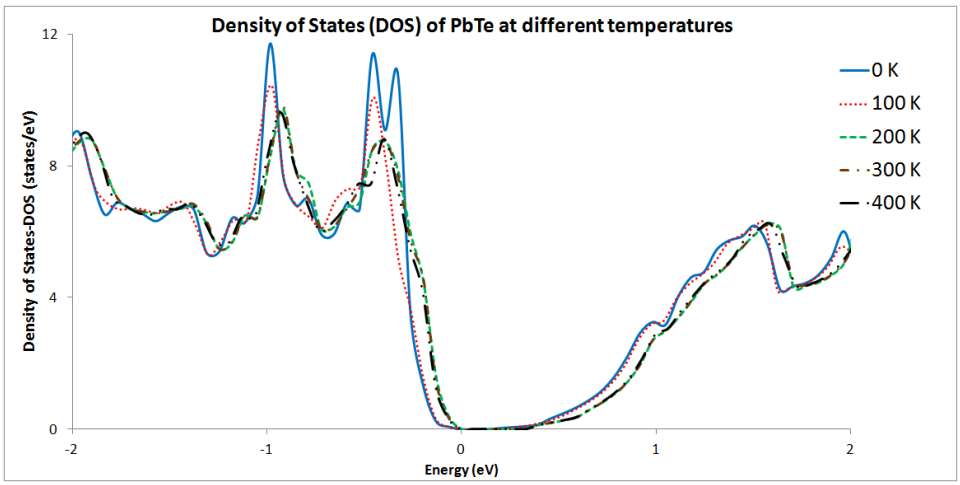

Figure 4.6: Density of States (DOS) of PbTe at different temperatures.

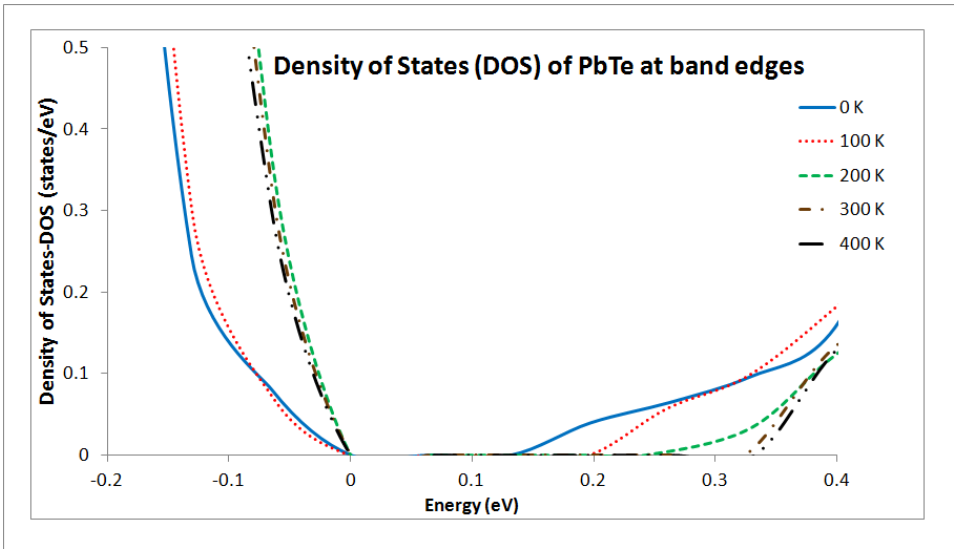

Figure 4.7: Density of States (DOS) of PbTe at the band edges.

Table 4.2: Comparison of calculated and experimental values for bandgap and displacement of Pb^{2+} ions.

Temperature in K	Experimental Bandgap[2] in eV	Calculated Bandgap in eV	Experimental Displacement of Pb^{2+} ions[8] in Å	Calculated Displacement of Pb^{2+} ions in Å		
				x	y	z
0	0.19	0.13	0	0	0	0
100	0.23	0.195	0.055	0.052	0.047	0.0098
200	0.274	0.262	0.145	0.1518	0.052	0.0036
300	0.316	0.328	0.18	0.164	0.0746	0.0042
400	0.358	0.334	0.22	0.185	0.108	0.06

From the DFT calculations we could determine the temperature dependence of energy bandgap of the material along with the stable structural configuration of the system at each temperature range by considering the thermal lattice expansion and the off-centering of Pb^{2+} ionic cores. Moreover, from the results we could confirm that the distortions of Pb^{2+} ions are predominant along x and there is moderate displacement along y and negligible displacement along z rather than only in <100> direction.

4.5 Effective mass of charge carriers vs. Temperature

Similar to the work on energy bandgap, the temperature dependence of effective masses of charge carriers is also determined from first principles DFT calculations. The expressions for conductivity effective masses of the charge carriers at different temperatures are given by Wagner [16].

$$m_c^* = 0.052 + 0.024\left(\frac{T_L}{300}\right) - 0.0027\left(\frac{T_L}{300}\right)^2$$

$$m_v^* = 0.056 + 0.027\left(\frac{T_L}{300}\right) - 0.0023\left(\frac{T_L}{300}\right)^2$$

where m_c^* and m_v^* are the conductivity effective masses of electrons and holes respectively and T_L is the lattice temperature. We use the band structure calculations at different temperatures to determine the effective mass of the carriers. The dispersion relation for two bands is given by Kane expression [17],

$$E(k) = \sqrt{\left(\frac{E_g}{2}\right)^2 + E_g\frac{\hbar^2 k^2}{2m^*}} - \frac{E_g}{2}$$

where E_g is the energy bandgap of the material, m^* is the conductivity effective mass of the charge carrier and k is the wave vector. We use the Kane expression and do curve fitting with the obtained energy band structure of the material at different temperatures to get the effective mass

of the carriers as shown in Fig. 4.8. (Red curves represent Kane energy dispersion and blue curves represent energy dispersion from DFT calculations). Our main area of interest is the band edges of the conduction and valence band because carriers in those energy levels primarily contribute to the transport properties of the material. From the band structure of PbTe at different temperatures we could see the enhancement of energy bandgap at the point L and the energy bands flatten out with increasing temperature, giving rise to higher conductivity effective masses of charge carriers. The conductivity effective masses of charge carriers are related to the curvature of energy band structure at the band edges by the following relation,

$$m^* = \frac{\hbar^2}{\frac{d^2E}{dk^2}}$$

where m^* is the conductivity effective mass of charge carrier, i.e. the effective mass of charge carrier is inversely proportional to the rate of change of slope of the energy band. Away from the band edges, we could see that the energy dispersion relation is almost linear which would be the case for a narrow bandgap semiconductor. This is attributed to the semi relativistic behavior of carriers in the energy bands as explained by Zawadzki et al. [18].

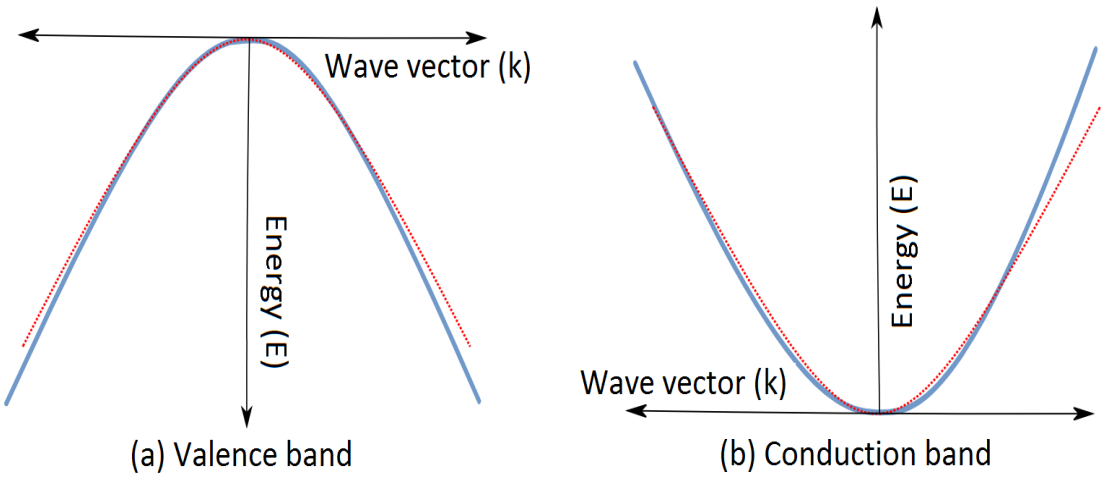

(i) 0 K

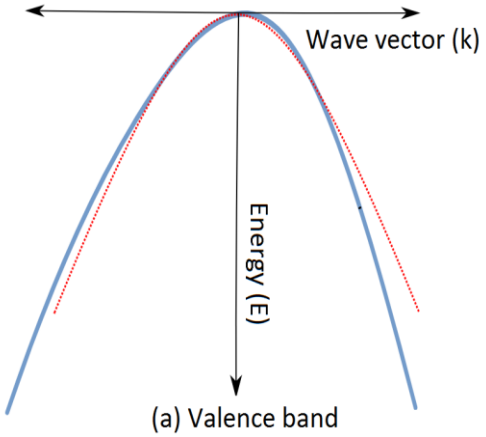

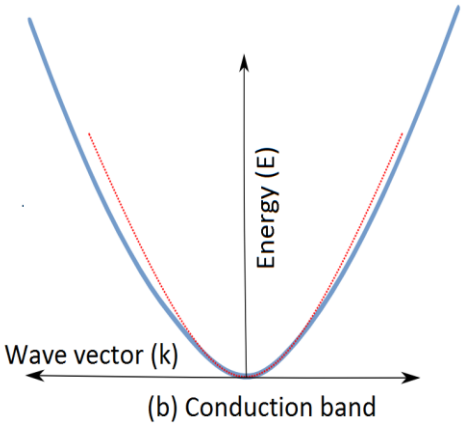

(ii) 100 K

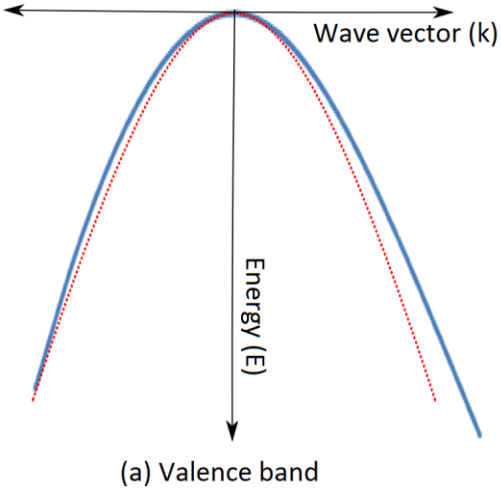

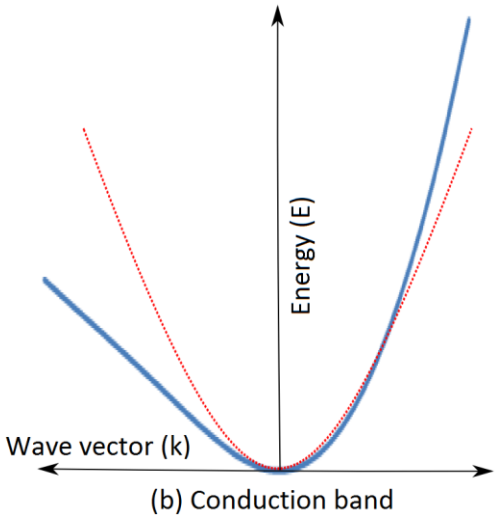

(iii) 200 K

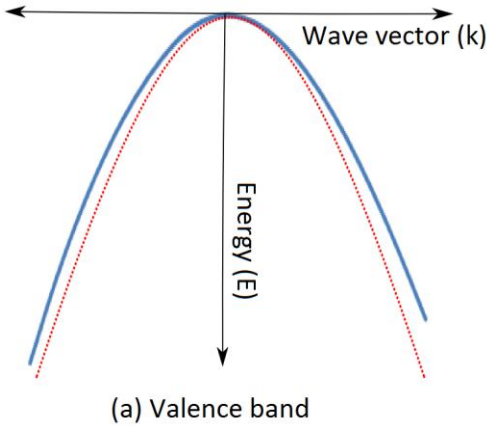

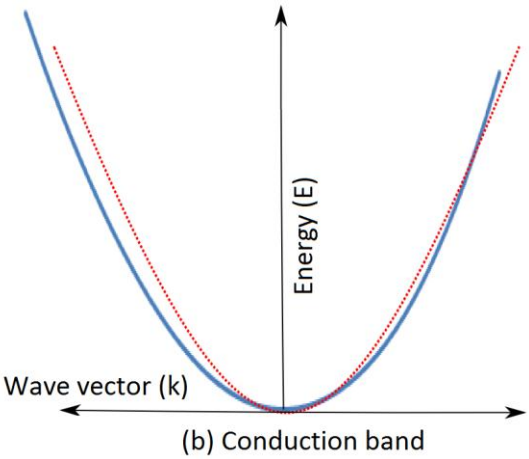

(iv) 300 K

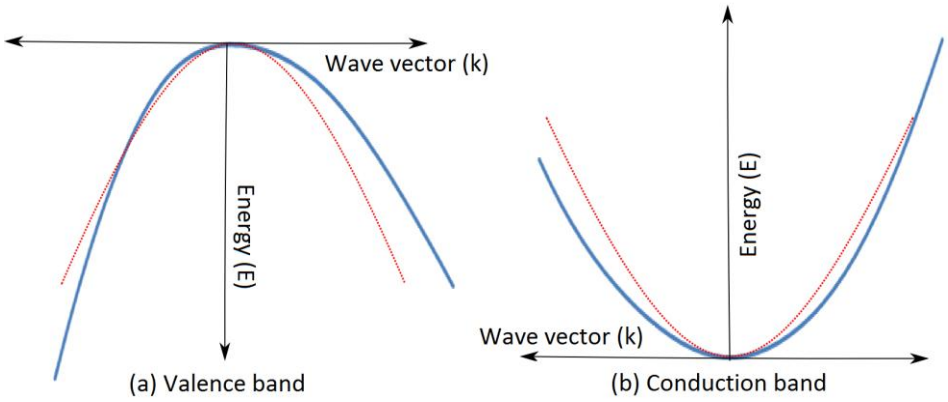

(v) 400 K

Figure 4.8: Curve fitting the band edges of PbTe at different temperatures (a) Valence Band (b) Conduction Band using the Kane dispersion relation

The band structure of PbTe at different temperature ranges from 0 K to 400 K is shown in Fig. 4.9. We could see the enhancement of direct bandgap at the point L with increase in temperature and also the energy curve flattens up at the band edges with rising temperature leading to higher effective masses of charge carriers. With higher effective masses, the mobility of charge carrier decreases. So with increase in temperature, the energy bands broaden leading to a higher effective mass and lower mobility of charge carriers.

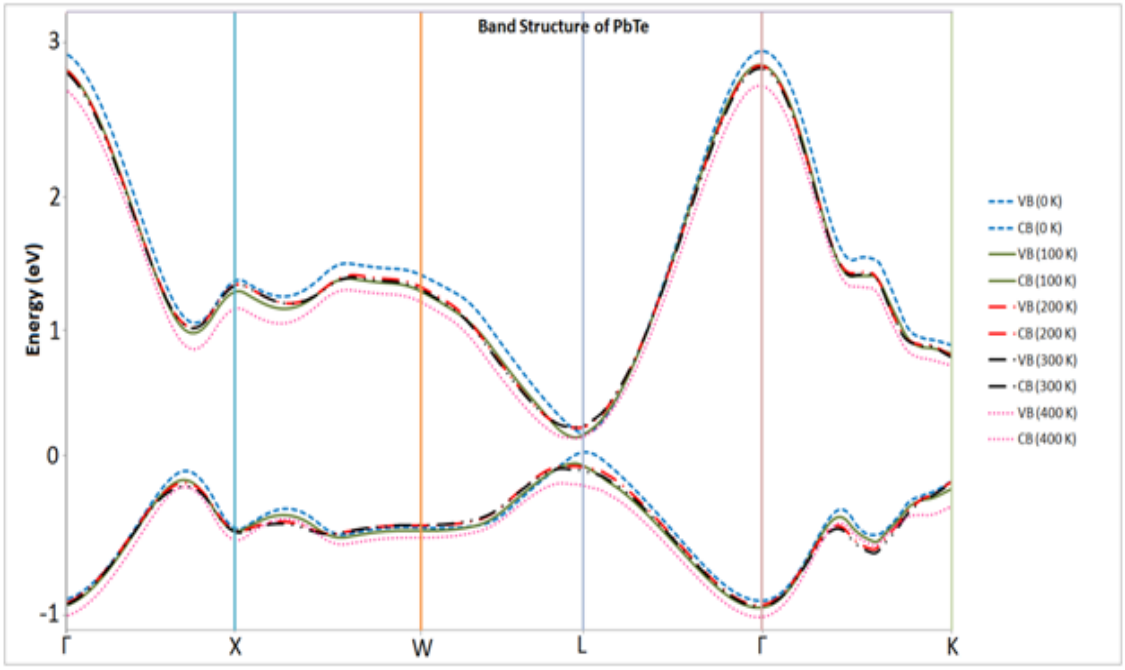

Figure 4.9: Band structure of PbTe at different temperatures

The conductivity effective mass of holes m_h^* and conductivity effective mass of electrons m_e^* at different temperatures as a ratio of free electron mass m_0 are tabulated as in Table 4.3 and we could see a linear behavior in the effective mass with temperature.

Table 4.3: Conductivity effective masses of carriers at different temperatures.

Temperature in K	**Conductivity effective mass of holes m_h^*/m_0**	**Conductivity effective mass of electrons m_e^*/m_0**
0	0.0635	0.0508
100	0.0704	0.0563
200	0.0782	0.0609
300	0.0824	0.0644
400	0.0894	0.0695

Wide ranges of values are found in the literature for effective masses of carriers for a given temperature, say at 300 K, the conductivity effective masses for holes range from 0.0743 to 0.10 m_0[16,19] and similarly for electrons 0.0607 to 0.13 m_0[20,21] . The effective mass of carriers in a material is very sensitive to temperature and purity of the material. The presence of impurities are primary sources of different scattering potentials that dominate scattering mechanisms at low temperatures and phonon generation at higher temperatures leading to complex interactions between carriers and the scattering sources. These interactions are responsible for the variation in effective masses of charge carriers at a given temperature.

The temperature dependence of conductivity effective mass of holes and electrons are compared with results from Wagner [16] and Landolt Bornstein [20] in Fig. 4.10.

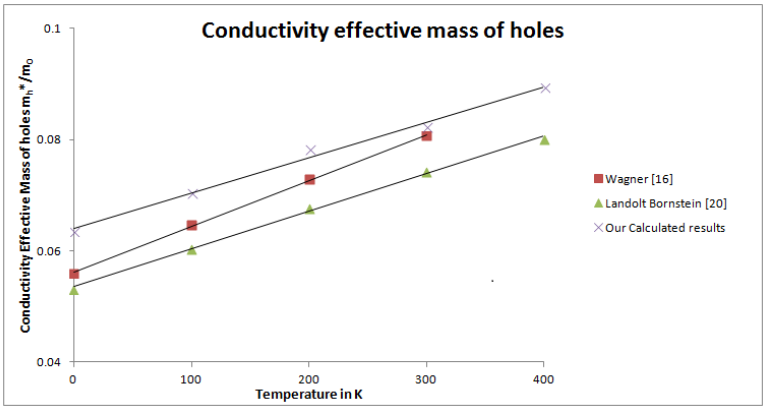

(a)

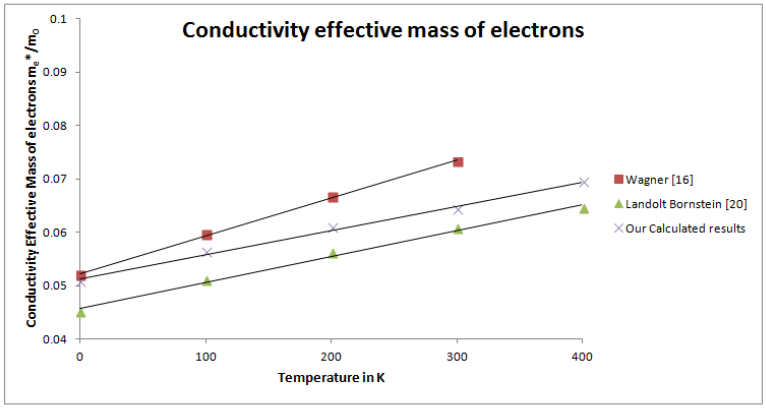

(b)

Figure 4.10: Variation of conductivity effective masses with temperature.

PbTe has a band valley degeneracy N_v of 4 [2] and from the conductivity effective masses ($m_i^* = m_h^*$ *or* m_e^*) we determine the total density of states effective mass of electrons (m_e) and holes (m_h) using the following relation.

$$m_i = N_v^{\frac{2}{3}} m_i^*$$

The total density of states effective mass also could be found by curve fitting the density of states obtained from DFT calculations. We use Kane two-band model that is commonly used in narrow bandgap semiconductors to determine the density of states.

The expression for density of states [5] for the two-band model is,

$$D\,(E) = \frac{\sqrt{2}\,N_v\,m_i^{*3/2}}{\pi^2\hbar^3}\sqrt{E\left(1+\frac{E}{E_g}\right)\left(1+2\frac{E}{E_g}\right)}$$

where m_i^* is the density of states effective mass for a single ellipsoid or the conductivity effective mass and N_v is the multiplicity of valleys and m_i is the total density of states effective mass of charge carriers. The above model was used to determine the total effective mass of the carriers at 0 K at the band edges. The fitting of density of states for 0 K is shown in Fig. 4.11.

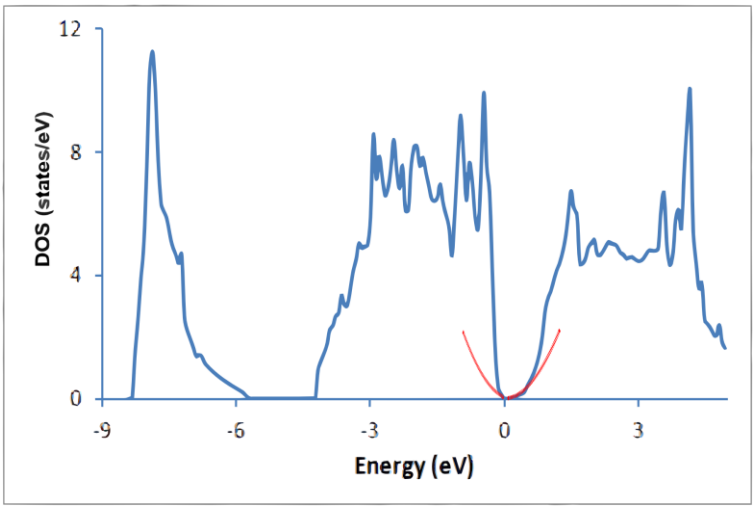

Figure 4.11: Curve fitting the density of states of PbTe at 0 K using the Kane two-band model.

The material has a Kane–like shape near the band edge which implies the density of states has approximately $\sqrt{E}$ dependence at the edges and at higher energies away from the band edge it has enhanced density of states because of non-parabolic nature of bands and quasi relativistic effects as discussed in the initial section. There is a limitation on the energy regime where Kane two-band model can be used. The expression for density of states from Kane two-band model can provide a good approximation within 0.1 eV ranges from the band edges because of non-parabolic nature of bands [5]. The valence band is very sensitive to temperature and the density of states in the valence band at higher temperatures is steeper even at the band edges and making it difficult to apply the Kane two-band model to determine the effective masses of the carriers.

The total density of states effective mass at different temperatures is calculated using the relation between conductivity effective mass and band valley degeneracy and are tabulated in Table 4.4.

Table 4.4: Total density of states effective masses of carriers at different temperatures.

Temperature in K	Total density of states Effective mass of holes m_h/m_0	Total density of states Effective mass of electrons m_e/m_0
0	0.1601	0.1280
100	0.1774	0.1419
200	0.1971	0.1535
300	0.2077	0.1622
400	0.2253	0.1750

The fitting of the density of states curves at 0 K is done using the expression from Kane two-band model and we obtain the total density of states effective masses as, $m_e = 0.1275\, m_0$ (where m_0 is the mass of free electron) for electrons which are in good agreement with the values from literature $m_e = 0.13\, m_0$ [22] and with the results from the band structure calculations in Table 4.4. The total density of states effective mass for holes is $m_h = 0.2679\, m_0$ which is slightly higher when compared to the values obtained from the band structure calculations. In the literature a wide range of values are found for the total density of states effective mass of holes ranging from $m_h = 0.14\, m_0$ to $0.31\, m_0$ [15, 21, 23–24]. The total density of states effective mass of electrons from density of states calculations is in good agreement with the results from band structure calculations. In the case of holes, the total density of states effective mass is higher when compared to the results from band structure calculations at 0 K. This discrepancy in the total density of states effective mass of holes might be attributed to the density of states fitting using Kane two-band model. This model gives an approximate expression for the density of states of the material and as we could see the density of states at the valence band edges rise steeply (highly non-parabolic) when compared to the conduction band edges, a good fit for the density of states was not achieved using the Kane two-band model. The

total density of states effective mass from our band structure calculations and from the values of Wagner [16] and Bornstein [20] are compared in Fig. 4.12.

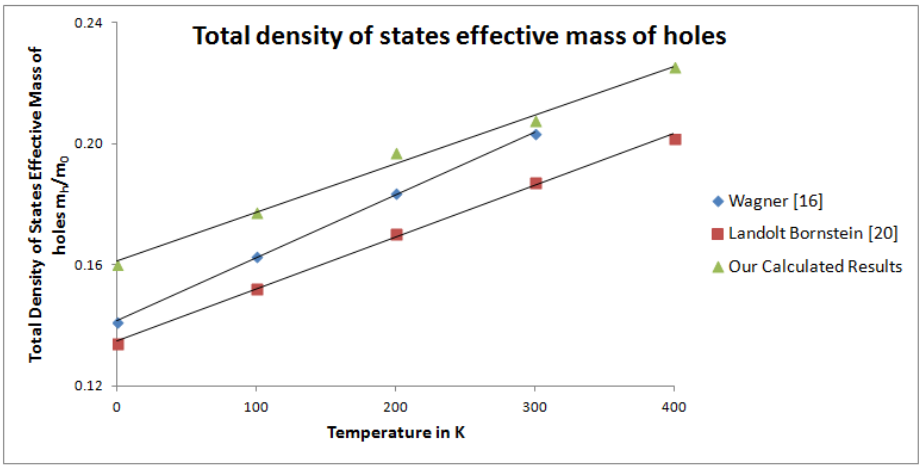

(a)

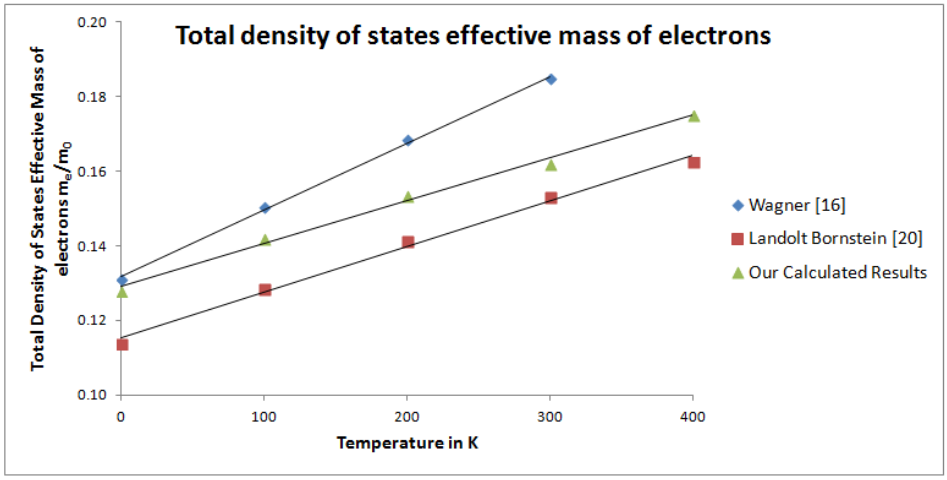

(b)

Figure 4.12: Total density of states effective mass (a) holes and (b) electrons.

4.6 Conclusion

The experimental work on formation of structural dipoles in lead chalcogenides predicted that the distortions of Pb^{2+} ionic cores were likely in the <100> direction [8]. Using the amplitude of distortions and by relaxing the system we find the stable configuration at different temperatures. From our results we conclude that the Pb^{2+} ions displace primarily in the x-direction and there is

moderate displacement along the y-direction and negligible displacements along the z-direction. Based on our band structure calculations at different temperatures we determined the effective masses of charge carriers. The enhancement in band gap of the material and increase in effective masses of the carriers are determined from DFT calculations by incorporating the lattice thermal expansion and lattice off centering of Pb^{2+} ions. The linear increase in effective mass even after 400 K is not determined from our calculations, which can be explained with the two-valence and single-conduction band model [25]. At low temperatures, the light valence band (L band) is dominating and at temperatures greater than approximately 450 K, the heavy valence band ($\sum$ band) which is 0.2 eV below the first valence band, dominates the hole transport leading to a higher thermoelectric power (α) and zT of 1.4 at 750 K in p-type PbTe materials [26].

The structural changes in the material are incorporated into our DFT calculations to determine the temperature effects on the electronic properties of the material such as the energy bandgap and effective mass of the charge carriers. The linear increase in effective mass of carriers even above 400 K could be explained by the two valence and single conduction band model [25] as well as by the pronounced carriers and phonons interactions at high temperatures. The complex interactions between phonons and charge carriers cannot be predicted from first principles DFT calculations.

4.7 References

1. Y. Zhang, X. Ke, C. Chen, J. Yang, P.R.C. Kent, Thermodynamic properties of PbTe, PbSe and PbS: First – principles study. *Physical Review B* **80**, 024304 (2009).
2. D.I. Bilc, S.D. Mahanti, M.G. Kanatzidis, Electronic transport properties of PbTe and $AgPb_mSbTe_{2+m}$ systems. *Physical Review B* **74**, 125202 (2006).
3. M. Lundstrom, Fundamentals of carrier transport. Cambridge University Press, Cambridge (2000).
4. E.O. Kane, Semiconductors and Semimetals, **1**, 75 – 100 (1966).
5. B.L. Huang, M. Kaviany, Ab initio and molecular dynamics predictions for electron and phonon transport in bismuth telluride. *Physical Review B* **77**, 125209 (2008).
6. Y.W. Tsang, M.L. Cohen, Calculation of the temperature dependence of the energy gaps in PbTe and SnTe. *Physical Review B* **3**, 1254 (1971).
7. C. Keffer, T.M. Hayes, A. Bienenstock, PbTe Debye – Waller factors and band – gap temperature dependence. *Physical Rev. Lett.* **21**, 1676 (1968)
8. E.S. Bozin, C.D. Malliakas, P. Souvatzis, T. Proffen, N.A. Spaldin, M.G. Kanatzidis, S.J.L. Bilinge, Entropically stabilized local dipole formation in lead chalcogenides. *Science* **330**, 1660 (2010).
9. G. Kresse, J. Furthmuller, Efficient iterative schemes for ab initio total – energy calculations using a plane – wave basis set. *Physical Review B* **54**, 11169 (1996).
10. G. Kresse, J. Furthmuller, Efficiency of ab – initio total energy calculations for metals and semiconductors using a plane – wave basis set. *Computational Materials Science* **6**, 15 (1996).
11. G. Kresse, D. Joubert, From ultrasoft pseudo-potentials to the projector augmented – wave method. *Physical Review B* **59**, 1758 (1999).
12. J.P. Perdew, Electronic Structure of Solids (Eds. Ziesche, P., Eschrig, H.), *Akademie Verlag:Berlin*. **11** (1991).
13. H.J. Monkhorst, J.D. Pack, Special points for Brillouin – zone integrations. *Physical Review B* **13**, 5188 (1976).

14. M. Methfessel, A.T. Paxton, High – precision sampling for Brillouin – zone integration in metals. *Physical Review B* **40**, 3616 (1989).

15. H.A. Lyden, Temperature dependence of the effective masses in PbTe. *Physical Review* **135**, A514 (1964).

16. *http://www.iue.tuwien.ac.at/phd/mwagner/diss.html*

17. E.O. Kane, Band structure of indium antimonide. *Journal of Physics and Chemistry of Solids* **1**, 249–261 (1957).

18. W.Zawadzki, S. Klahn, U.Merkt, Semirelativistic behavior of electrons in InSb in crossed magnetic and electric fields. *Physical Review Letters* **55**, 983–986 (1985).

19. N. Piccioli, J.M. Besson, M. Balkanski, Optical constants and bandgap of PbTe from thin film studies between 25 and 300 °K. *Journal of Physics and Chemistry of Solids* **35**, 971–977 (1974).

20. Landolt–Börnstein – Group III Condensed Matter Volume **41C**, 1 – 3 (1998).

21. A.K. Walton, T.S. Moss, B. Ellis, Determination of the Electron Effective Mass in the Lead Salts by the Infra-red Faraday Effect. *Proceedings of the Physical Society* **79**, 1065–1068 (1962).

22. G. Martinez, M. Schluter, M.L. Cohen, Electronic structure of PbSe and PbTe. I. Band structures, densities of states and effective masses. *Physical Review B* **11**, 651 (1975).

23. J.B. Conklin, L.E. Johnson, G.W. Pratt,Jr, Energy bands in PbTe. *Phys. Rev* **137,** A1282 (1965).

24. I.A. Chernik, V.I. Kaidanov, M.I. Vinogradova, N.V. Kolomoets, Investigation of the valence band of lead telluride using transport phenomena. *Soviet Physics – Semiconductors* **2**, 645–651 (1968).

25. R.N. Tauber, A.A. Machonis, I.B. Cadoff, Thermal and Optical Energy gaps in PbTe. *J.Appl. Phys*. **37**, 4855 (1966).

26. Y. Pei, N.A. Heinz, A. LaLonde, G.J. Snyder, Combination of large nanostructures and complex band structure for high performance thermoelectric lead telluride. *Energy Environ. Sci.* **4**, 3640 – 3645 (2011).

5 Determination of carrier scattering relaxation time in PbTe

This section on determination of charge carrier scattering relaxation time in PbTe deals with the method employed in calculating the charge carrier scattering time, which is one of the primary factors used in determining the thermoelectric transport properties of the material. This chapter outlines the dominant carrier scattering sources present in the material and also discusses the analytical expressions involved in determining the carrier scattering time from these different scattering sources. The results obtained from the previous section like the energy bandgap and effective masses of the charge carriers are used in calculating these scattering rates.

5.1 Charge carrier transport in materials

The charge carriers in metals and semiconductors are affected by applied external fields like electric, magnetic fields and also by temperature gradients across the system [1]. This affects the equilibrium of the system and the carriers have a net nonzero momentum. Generally, there are three types of effects that are to be considered in carrier transport across the material that affects the probability distribution function of the particle namely diffusion, external fields and scattering.

5.2 Charge carrier scattering relaxation time

The scattering of charge carriers in the material is a key factor that determines the transport properties of the material under consideration. We calculate the charge carrier scattering relaxation time, which is the mean time between two scattering events based on the assumption that there are only elastic scattering of charge carriers.

The mean time between two scattering events, which is termed as charge carrier scattering relaxation time (τ), is used in determining the mobility of charge carriers across the material. If the scattering time is less i.e. the probability of charge carrier scattering is higher, then the mobility of carriers is also less, which affects the conductivity of the material. This could be explained by the following expression,

$$\mu = \frac{e\tau}{m^*}$$

where μ is the mobility of charge carrier in terms of scattering relaxation time τ, charge of the carrier e and effective mass of the charge carrier m^*. This relaxation time τ is used in determining the transport properties like Seebeck coefficient and electrical conductivity of the material. The expressions for the carrier concentration, Seebeck coefficient (α) and electrical conductivity (σ) are defined as in [2].

$$\alpha = \frac{1}{eT} \frac{\int_0^\infty -\frac{\partial f}{\partial \epsilon} (\epsilon - \mu) \left[\epsilon(1 + \frac{\epsilon}{E_g}\right]^{3/2} \left(1 + \frac{2\epsilon}{E_g}\right)^{-1} \tau_\epsilon \, d\epsilon}{\int_0^\infty -\frac{\partial f}{\partial \epsilon} \left[\epsilon(1 + \frac{\epsilon}{E_g})\right]^{3/2} \left(1 + \frac{2\epsilon}{E_g}\right)^{-1} \tau_\epsilon \, d\epsilon}$$

The electrical conductivity of the material is given by,

$$\sigma = \frac{2}{3} N_v e^2 (2m_i^*)^{1/2} \int_0^\infty -\frac{\partial f}{\partial \epsilon} \left[\epsilon(1 + \frac{\epsilon}{E_g})\right]^{3/2} \left(1 + \frac{2\epsilon}{E_g}\right)^{-1} \tau_\epsilon \, d\epsilon$$

Similarly, the expression for carrier concentration (n) in terms of carrier effective masses is given by,

$$n = \frac{\sqrt{2}\, N_v\, m_i^{*3/2}}{\pi^2 \hbar^3} \int_0^\infty \frac{\left[\epsilon(1 + \frac{\epsilon}{E_g})\right]^{1/2} \left(1 + \frac{2\epsilon}{E_g}\right) d\epsilon}{e^{\left(\frac{\epsilon - \mu}{k_B T}\right)} + 1}$$

where e is the electronic charge, T is the temperature, f is the Fermi–Dirac distribution function, ϵ is the energy level of the system, E_g is the energy bandgap of the material, τ_ϵ is the scattering

relaxation time at the given energy ϵ, N_v is the band valley degeneracy, ħ is the reduced Planck's constant and m_i^* is the conductivity effective mass of the charge carrier.

The effective masses of charge carriers and the energy bandgap of the material computed from the last section along with the total scattering relaxation time τ_ϵ are employed in determining the above transport properties of the material at different temperatures. It could be seen that Seebeck coefficient and the electrical conductivity of the material depends on the total scattering relaxation time. The relaxation time is a function of energy. In the following section we define the different scattering mechanisms that are applicable to our system and the expressions that are used to calculate the different relaxation times are discussed in detail.

5.3 Scattering mechanism in charge carriers

The expressions for transport properties have the total scattering relaxation time; τ_ϵ and this function could be obtained by summing up the individual scattering rates τ_i.

$$\tau_\epsilon{}^{-1} = \sum_i \tau_i{}^{-1}$$

The dominant charge scattering mechanisms in PbTe are scattering by vacancies (point defects) and by phonons. At low temperatures, charge carriers are mostly scattered by vacancies and as the temperature increases, the effect of vacancy scattering is less predominant and scattering by phonons dominate [3]. At low temperatures and low carrier densities on the order of $5\text{x}10^{18}\ cm^{-3}$,scattering by coulomb potential of vacancies dominate and at higher carrier densities, the Coulomb potential of vacancies are screened and scattering by short range potential of vacancies is predominant [3]. At considerable temperatures (room temperatures and higher) atoms vibrate at their equilibrium sites generating phonons that can induce volume changes in the lattice structure of the material and thereby altering the periodicity of the lattice. These

vibrations scatter the charge carriers. The schematic representation of charge carrier scattering is shown in Fig. 5.1

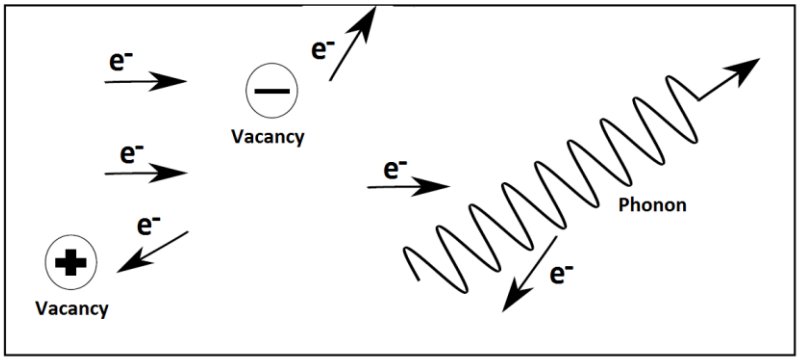

Figure 5.1: Schematic representation of few charge carrier scattering mechanisms inside a material.

The phonons generated are of two types namely acoustic and optical phonons. Acoustic phonons are generated due to the coherent movement of atoms out of their equilibrium position in the lattice. Optical phonons are found in materials with more than one type of atoms. These types of phonons are generated by the out-of-phase movement of atoms from their equilibrium positions and they occur because of the uneven charge distribution between different atoms that occupy the crystal lattice. At room temperatures and higher, scattering by acoustic phonons and optical phonons contribute mainly to the total scattering relaxation time [3].

There are five common charge scattering mechanisms that are considered in determination of the total scattering relaxation time as a function of energy namely, deformation potential of the acoustic phonons, deformation potential of the optical phonons, polar scattering by optical phonons (coupled system of electron and longitudinal optical phonon), short range deformation potential of vacancies and Coulomb potential of vacancies.

5.3.1 Scattering by deformation potential of acoustic phonons

For electrons the relaxation time for acoustic deformation potential scattering using Kane model of dispersion and assuming elastic scattering is given by [2],

$$\tau_a = \frac{\tau_{0,a}(T)\left(\epsilon + \frac{\epsilon^2}{E_g}\right)^{-1/2}}{\left(1 + 2\frac{\epsilon}{E_g}\right)[(1-A)^2 - B]}$$

$$A = \frac{\frac{\epsilon}{E_g}(1 - K_a)}{\left(1 + 2\frac{\epsilon}{E_g}\right)}$$

$$B = \frac{8\frac{\epsilon}{E_g}\left(1 + \frac{\epsilon}{E_g}\right)K_a}{3\left(1 + 2\frac{\epsilon}{E_g}\right)^2}$$

$$\tau_{0,a}(T) = \frac{2\pi\hbar^4 C_l}{{E_{ac}}^2 k_B T\,(2m_i^*)^{3/2}}$$

where, E_{ac} is the acoustic deformation potential coupling constant for the conduction band C_l is a combination of elastic constant, $K_a = \frac{E_{av}}{E_{ac}}$ is the ratio of acoustic deformation potential coupling constants for valence and conduction bands.

5.3.2 Scattering by deformation potential of optical phonons

The scattering by deformation potential of optical phonons is similar to the acoustic phonons and the expression for relaxation time is given by [2],

$$\tau_o = \frac{\tau_{0,o}(T)\left(\epsilon + \frac{\epsilon^2}{E_g}\right)^{-1/2}}{\left(1 + 2\frac{\epsilon}{E_g}\right)[(1-A)^2 - B]}$$

$$A = \frac{\frac{\epsilon}{E_g}\,(1 - K_o)}{\left(1 + 2\frac{\epsilon}{E_g}\right)}$$

$$B = \frac{8\frac{\epsilon}{E_g}\left(1 + \frac{\epsilon}{E_g}\right)K_o}{3\left(1 + 2\frac{\epsilon}{E_g}\right)^2}$$

$$\tau_{0,o}(T) = \frac{2\hbar^2 a^2 \rho(\hbar\omega_0)^2}{\pi {E_{oc}}^2 k_B T\,(2m_i^*)^{3/2}}$$

where, E_{oc} is the optical deformation potential coupling constant for the conduction band, a is the lattice parameter of the crystal, ρ is the density of the material, ω_0 is the optical phonon frequency and $K_o = \frac{E_{ov}}{E_{oc}}$ is the ratio of optical deformation potential coupling constants for valence and conduction bands.

5.3.3 Scattering by polar optical phonons

The relaxation time polar optical phonons is given by [2],

$$\tau_{po} = \frac{\hbar^2\left(\epsilon + \frac{\epsilon^2}{E_g}\right)^{1/2} F^{-1}}{e^2(2m_i^*)^{1/2}k_B T(\varepsilon_\infty^{-1} - \varepsilon_0^{-1})\left(1 + 2\frac{\epsilon}{E_g}\right)}$$

$$F = 1 - \delta ln(1 + \delta^{-1}) - \left\{\frac{2\frac{\epsilon}{E_g}\left(1 + \frac{\epsilon}{E_g}\right)}{\left(1 + 2\frac{\epsilon}{E_g}\right)^2}[1 - 2\delta + 2\delta^2 ln(1 + \delta^{-1})]\right\}$$

$$\delta = (2kr_0)^2$$

where ε_0 and ε_∞ are the static and high frequency relative permitivities, k is the carrier wave vector and r_0 is the screening length of the optical phonons.

$$k^2 = \frac{2m_i^* \left(\epsilon + \frac{\epsilon^2}{E_g}\right)}{\hbar^2}$$

$${r_0}^{-2} = \frac{2^{5/2}(m_i)^{3/2}e^2\left(\epsilon + \frac{\epsilon^2}{E_g}\right)}{\pi\hbar^3\varepsilon_\infty} \int_0^\infty -\frac{\partial f}{\partial \epsilon}\left[\epsilon(1+\frac{\epsilon}{E_g})\right]^{1/2}\left(1+\frac{2\epsilon}{E_g}\right)^1 d\epsilon$$

where m_i is the total density of states effective mass of the charge carriers.

5.3.4 Scattering by short range deformation potential of vacancies

The expression for relaxation time for this type of scattering is similar to that of electron – acoustic phonon scattering because they have similar deformation potential. The expression is given as [2]

$$\tau_v = \frac{\tau_{0,v}(T)\left(\epsilon + \frac{\epsilon^2}{E_g}\right)^{-1/2}}{\left(1+2\frac{\epsilon}{E_g}\right)[(1-A)^2 - B]}$$

$$A = \frac{\frac{\epsilon}{E_g}(1-K_v)}{\left(1+2\frac{\epsilon}{E_g}\right)}$$

$$B = \frac{8\frac{\epsilon}{E_g}\left(1+\frac{\epsilon}{E_g}\right)K_v}{3\left(1+2\frac{\epsilon}{E_g}\right)^2}$$

$$\tau_{0,v}(T) = \frac{\pi\hbar^4}{{U_{vc}}^2 N_{vac} m_i^* (2m_i^*)^{1/2}}$$

where, U_{vc} is the vacancy deformation potential coupling constant for the conduction band , N_{vac} is the vacancy density which depends on temperature. The procedure for determining the vacancy density is outlined in the following section. $K_v = \frac{U_{vv}}{U_{vc}}$ is the ratio of vacancy deformation potential coupling constants for valence and conduction bands.

5.3.5 Scattering by Coulomb potential of vacancies

The expression for relaxation time due to scattering by Coulomb potential of vacancies is given by [2],

$$\tau_C = \frac{\varepsilon_0^2 (2m_i^*)^{1/2} \left(\epsilon + \frac{\epsilon^2}{E_g}\right)^{3/2}}{\pi (Ze^2)^2 N_{vac} \left[ln(1+\xi) - \frac{\xi}{(1+\xi)}\right]\left(1 + 2\frac{\epsilon}{E_g}\right)}$$

$$\xi = (2kr_v)^2$$

where Ze is the vacancy charge and r_v is the screening radius of the vacancy potential. The expression for screening radius of vacancy potential is given as,

$$r_v{}^{-2} = \frac{4\pi e^2}{\varepsilon_0} D(\mu)$$

$$D(\mu) = \frac{\sqrt{2}\ m_i^{*3/2}}{\pi^2 \hbar^3} \sqrt{\mu\left(1 + \frac{\mu}{E_g}\right)}\left(1 + 2\frac{\mu}{E_g}\right)$$

where $D(\mu)$ is the density of states at the chemical potential μ

5.3.6 Total scattering relaxation time

Using the above relaxation times, the total scattering relaxation time is calculated using Matthiessen's rule which assumes that individual scattering probabilities are independent of each other.

$$\frac{1}{\tau_\epsilon} = \frac{1}{\tau_a} + \frac{1}{\tau_o} + \frac{1}{\tau_{po}} + \frac{1}{\tau_v} + \frac{1}{\tau_C}$$

The parameters that are used to calculate the relaxation times for PbTe at 4.2 K and 300 K [3] are given in the Table 5.1. The chemical potential of PbTe that we used in our calculation is taken from the work by Mahanti et al. [4]. The values for the chemical potential μ at different

temperatures and fixed carrier concentration at $n = 5\text{x}10^{19}\ cm^{-3}$ are extrapolated based on the equation from [4] and is expressed as

$$\mu(T) = A + BT^{C}$$

$$A = 0.17 \pm 0.001; B = -2.75\text{x}10^{-6} \pm 2.6\text{x}10^{-7}; C = 1.61 \pm 0.01$$

Table 5.1: Parameter table for PbTe at 4.2 K and 300 K.

Parameter	**Description**	**Unit of measurement**	**4.2 K**	**300 K**
m_l/m	Ratio of effective masses	-	0.24	0.24
m_t/m	Ratio of effective masses	-	0.026	0.0453
ε_0	Static permittivity	-	1470	400
ε_∞	High frequency permittivity	-	38.5	32.6
C_l	Combination of elastic constants	N/m^2	$0.81\text{x}10^{11}$	$0.71\text{x}10^{11}$
$\hbar\omega_0$	Energy of optical phonons	eV		0.0136
a	Lattice parameter of PbTe	Å	6.556	6.6046
ρ	Density	g/cm^3	8.24	8.24
Z	Vacancy charge	-	0.14	
E_{ac}	Acoustic deformation potential coupling constant for conduction band	eV	15	15
E_{oc}	Optical deformation potential coupling constant for conduction band	eV		26
U_{vc}	Deformation potential coupling constant of vacancies for conduction band	$ergs\ cm^3$	$3\text{x}10^{-34}$	$3\text{x}10^{-34}$

Parameter	Description	Unit of measurement	4.2 K	300 K
K_a, K_v, K_o	Ratio of potential coupling constants (for n – type)	-	1.0	1.0
K_a, K_v, K_o	Ratio of potential coupling constants (for p – type)	-	1.5	1.5
E_g	Energy band gap	eV	0.13	0.328

The vacancy density strongly depends on the temperature and we determine it from vacancy formation energy. The formation energies were determined by Hin et al. using first principles calculations. The formation energy of Pb vacancies is 0.59 eV and of Te vacancies is 0.99 eV in PbTe [5]. This implies Pb vacancies are easier to form than Te vacancies. Using the formation energy we determine the equilibrium vacancy concentration using the following expression

$$C_{vac} = e^{-\left(\frac{E_{vac}^{f}}{k_B T}\right)}$$

where C_{vac} is the vacancy concentration, E_{vac}^{f} is the vacancy formation energy, k_B is the Boltzmann's constant and T is the temperature. Using the above expression, the computed vacancy densities at different temperatures are listed in Table 5.2. The relation between vacancy density and carrier concentration [3] is given by

$$N_v = {}^{n}/_{2}$$

where N_v is the vacancy density and n is the carrier concentration of the material. The above relation could not be used in our case to determine the carrier concentration in the desired temperature range because; the vacancy concentration is very low at low temperatures. Hence,

the carrier concentration from vacancy densities cannot be used to determine the chemical potential of the material at different temperatures.

Table 5.2: Vacancy density at different temperatures

Temperature in K	Vacancy density m^{-3}
100	0.0518
200	3.79304×10^{13}
300	3.40397×10^{18}
400	1.0166×10^{21}

Using the parameter values at those temperatures, results from our ab–initio calculations, values for chemical potential [4] and the computed vacancy densities using vacancy formation energy [5], we determine the total scattering relaxation time at different temperatures. The trend of total scattering relaxation time with temperature is shown in Fig. 5.2

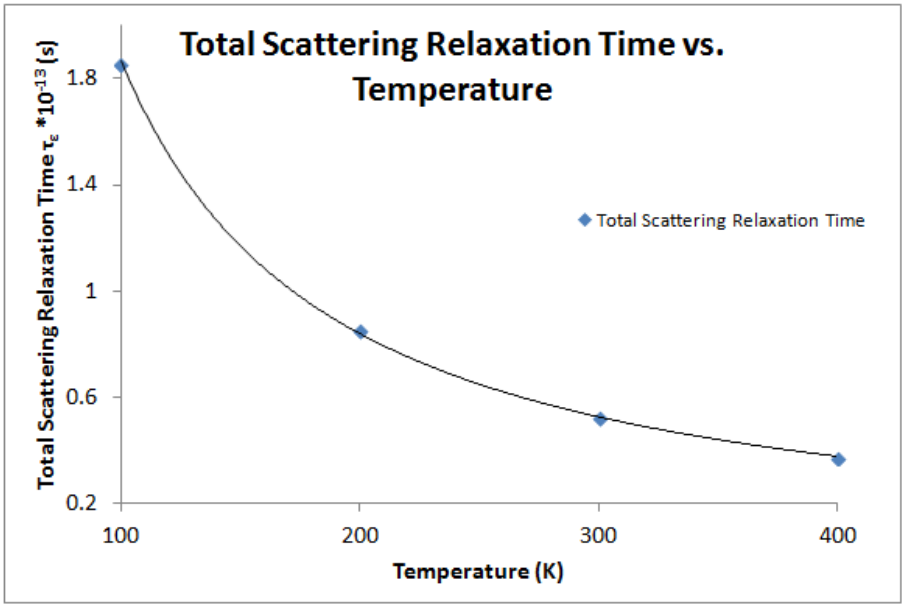

Figure 5.2: Variation of total scattering relaxation time with temperature.

The temperature dependence of the total relaxation scattering relaxation time of PbTe in the specified temperature range (100 K to 400 K) can be represented by the fitted expression as,

$$\tau_{\epsilon} = aT^{b}$$

where τ_{ϵ} is the total scattering relaxation time in s, T is the temperature in K, $a = 3.7814\text{x}10^{-11}$ and $b = -1.153$ are the fitting parameters.

The values for individual scattering relaxation time at 300 K and in the charge carrier energy range of 0.1 eV is compared in Table 5.3

Table 5.3: Comparison of individual scattering relaxation time in PbTe at 300 K.

Scattering Mechanism	**Calculated scattering relaxation time in s**	**Reference scattering relaxation time[2] in s**
Acoustic Phonons τ_a	$0.4174\text{x}10^{-12}$	$0.15 - 2.9\text{x}10^{-12}$
Optical Phonons τ_o	$0.3043\text{x}10^{-12}$	$0.18 - 2.0\text{x}10^{-12}$
Polar-Optical Phonons τ_{po}	$0.075\text{x}10^{-12}$	$0.1 - 0.19\text{x}10^{-12}$
Short range vacancies τ_v	$4.591\text{x}10^{-5}$	$2.4 - 44.7\text{x}10^{-12}$
Coulombic potential of vacancies τ_C	$3.083\text{x}10^{-5}$	$5.2 – 1216\text{x}10^{-12}$

The individual carrier scattering relaxation time at different temperatures in the charge carrier energy level of 0.1 eV is shown in Table 5.4.

Table 5.4: Relaxation time of different scattering mechanisms in PbTe.

Temperature K	τ_a s	τ_o s	τ_{po} s	τ_v s	τ_C s
100	$1.347\text{x}10^{-12}$	$0.973\text{x}10^{-12}$	$0.2771\text{x}10^{-12}$	$3.24\text{x}10^{15}$	$2.21\text{x}10^{15}$
200	$0.6514\text{x}10^{-12}$	$0.4727\text{x}10^{-12}$	$0.124\text{x}10^{-12}$	4.286	2.884
300	$0.4174\text{x}10^{-12}$	$0.3043\text{x}10^{-12}$	$0.0752\text{x}10^{-12}$	$4.591\text{x}10^{-5}$	$3.083\text{x}10^{-5}$
400	$0.2801\text{x}10^{-12}$	$0.2050\text{x}10^{-12}$	$0.0552\text{x}10^{-12}$	$1.37\text{x}10^{-7}$	$1.03\text{x}10^{-7}$

From the above table we could see that as the temperature increases the scattering relaxation time for different scattering mechanisms have a decreasing trend. This explains that at elevated temperatures the probability of charge scattering is high and hence, the mean time between the scattering events is less. Moreover, at all the temperature ranges under consideration, it could be seen that the dominant scattering mechanisms are by phonons, but this is not the case as explained by Zayachuk et al. [3]. This could be explained by the temperature dependence of vacancy concentration. We could see that the vacancy density plays a very important role in determining the carrier scattering time by short range vacancy potential and Coulombic potential of vacancies. The vacancy concentration increases exponentially with temperature. The comparison for individual scattering time at 300 K with the results from Mahanti et al. [2] also shows a huge variation in scattering time by vacancies because, a constant value for the vacancy density of $2\text{x}10^{24}\ m^{-3}$ was used and the temperature dependence was not accounted for. Moreover, we determined the chemical potential as a function of temperature at a fixed carrier concentration of $5\text{x}10^{19}\ cm^{-3}$. The temperature dependence of carrier concentration was not accounted when determining the chemical potential of the material.

5.4 Conclusion

By incorporating the temperature dependence of effective masses of charge carriers, energy bandgap and lattice parameter of PbTe, we determined the total scattering relaxation time in the charge carrier energy range of 0.1 eV. In Table 5.3 we compare our calculated results with results available in the literature and the individual scattering relaxation times for the phonons are in good agreement. There is a considerable variation when comparing the scattering relaxation time for short-range vacancies and Coulombic potential of vacancies because the vacancy concentration which is strongly dependent on temperature was assumed in the literature to be constant throughout. But in reality, the vacancy density increases with temperature. We incorporated this temperature dependence and we could see that at low temperatures, the scattering times for vacancies are many orders of magnitude higher. This implies that at those temperatures also the predominant scattering mechanism is through phonons because the vacancy concentration is a lot less at low temperatures and do not play a role in charge carrier scattering when compared to the phonons. Based on a discussion by Zayachuck [3], the scattering by Coulombic potential of vacancies are dominant at low temperature and at low carrier concentration levels and the scattering by the short range potential of vacancies are dominant at low temperatures and high carrier concentration levels. However, incorporating the vacancy concentration in our calculations, we could see that the vacancy density is a lot less at low temperatures and significantly higher at high temperatures. This implies scattering of charge carriers by vacancies also increases with increases in temperature. Moreover, parameters used in our calculations like deformation potential coupling constants are determined at 300 K and are assumed constant for the entire temperature range even though they depend on the temperature of the system. The chemical potential used for all the temperature ranges was calculated for a

fixed carrier concentration, but the carrier concentration is also dependent on temperature. Thus results from our ab–initio calculations and the vacancy density calculations are used to capture the temperature dependence of charge carrier scattering time at the desired charge carrier energy range.

5.5 References

1. J.M. Ziman, Principles of the theory of solids. Cambridge University Press, Cambridge (1972).
2. D.I. Bilc, S.D. Mahanti, M.G. Kanatzidis, Electronic transport properties of PbTe and $AgPb_mSbTe_{2+m}$ systems. *Physical Review B* **74**, 125202 (2006).
3. D.M. Zayachuk, The dominant mechanisms of charge – carrier scattering in lead telluride. *Semiconductors* **31**, 173 (1997).
4. S.Ahmad, S.D. Mahanti, Energy and temperature dependence of relaxation time and Wiedemann–Franz law on PbTe. *Physical Review B* **81**, 165203 (2010).
5. C.Hin, M.Dresselhaus, Z.Ren, G.Chen, Point defects in PbTe alloys. (Not published)

6 Interface energy calculations and band alignment

This chapter on interface energy calculations and band alignment describes the methodology involved in evaluating the flat surface interface energies between two compounds and determining the equilibrium crystal shape of the precipitate inside the host matrix using the Wulff construction [1]. The chapter outlines the types of semiconductor heterojunctions and the application of first principles DFT calculations in electronic energy band offset engineering. It also describes the relation developed between the interface energies and electronic energy band offsets.

6.1 Interface energy calculations

The SrTe precipitate and PbTe host matrix interface energies are calculated at 0 K from first principles DFT calculations using VASP. Two flat surfaces of PbTe and SrTe are considered as shown in Fig. 6.1. These surfaces are placed side by side to create PbTe/SrTe interface. PbTe, SrTe and $Pb_{1-x}Sr_xTe$ have the same rocksalt structure with the same space group ($Fm\bar{3}m$).

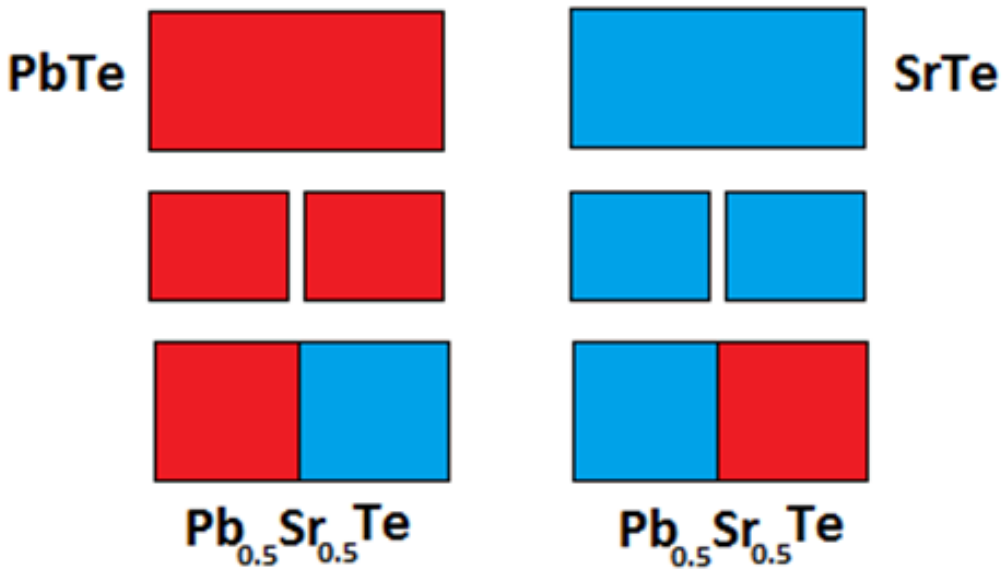

Figure 6.1: Representation of flat interface between PbTe and SrTe compounds.

The interface energy between the precipitate and host matrix is given by,

$$\gamma = \frac{\Delta E}{2S}$$

$$\Delta E = E_{Pb_{0.5}Sr_{0.5}Te} - \frac{1}{2}(E_{PbTe} + E_{SrTe})$$

where γ is the interface energy in mJ/m^2, ΔE is the difference in energy between the combined and individual systems in mJ and S is the surface area of the interface in m^2.

The interface energies for different interface orientations were calculated as a function of number of planes of atoms used in the DFT calculations. The [100], [110] and [111] interfaces with 6 planes of atoms on either side of the interface is shown in Fig. 6.2

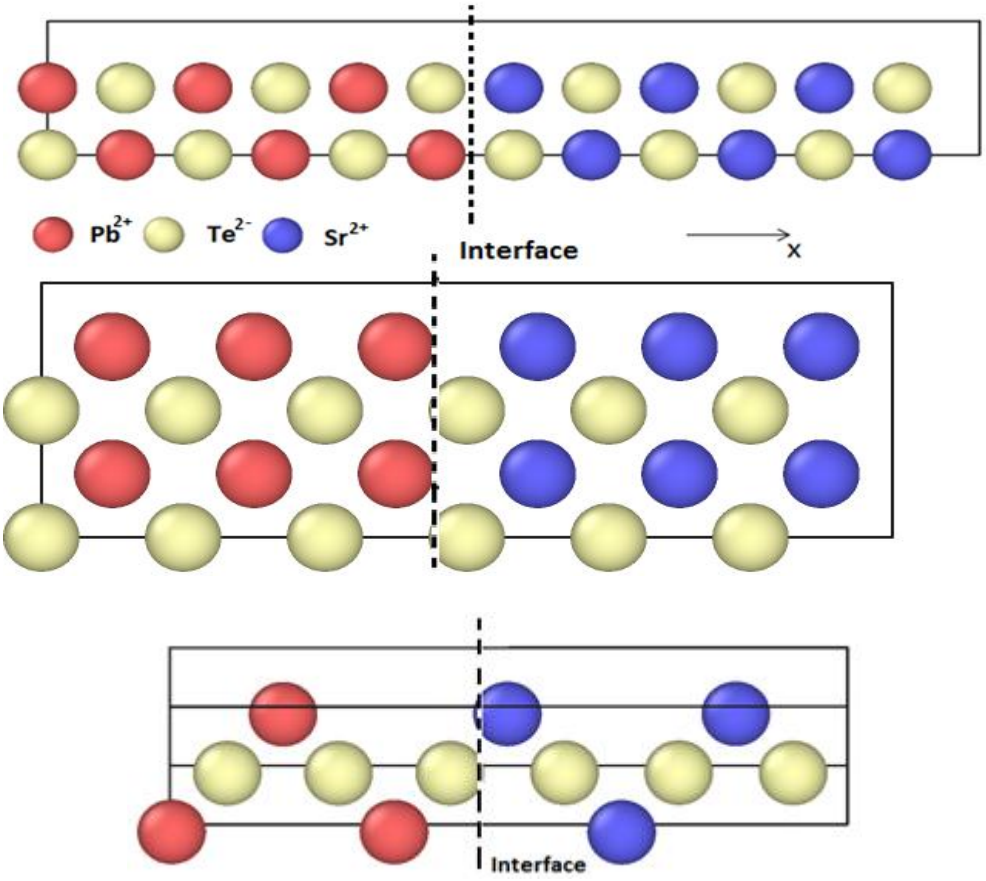

Figure 6.2: Front view of [100], [110] and [111] PbTe/SrTe interface with 6 planes of atoms on each side.

The interface energies of PbTe/SrTe system for different orientations and for different number of planes are tabulated in Table 6.1.

Table 6.1: Interface Energies of $Pb_{0.5}Sr_{0.5}Te$ for different interface orientations

Interface	Interface Energy in mJ/m^2 (4 planes each)	Interface Energy in mJ/m^2 (6 planes each)
[100]	1.71	1.38
[110]	1.97	1.59
[111]	9.89	8.01

From the table we could see that the interface energies of the material decrease with the increase in number of planes used in DFT calculations. Higher interface energies with fewer planes of atoms might be attributed to the interaction between two interfaces. The periodicity of the crystal is maintained in the VASP simulation box and the [100] interface repeats after every set of 4 or 6 planes based on the input provided. So, a large number of plane of atoms are required on either side of the interface to accurately determine the interface energies. Due to computational limitations we used a set of 6 planes of atoms on each side of the interface for the calculations.

The interface energies between the precipitates and host matrix are used in determining the crystal shape of the SrTe precipitates that are embedded in the PbTe matrix. We see that the [100] interface has the lowest energy amongst the three interface orientations. The predominant shape of the precipitate has the orientation with lowest interface energies

6.2 Determination of equilibrium crystal shape

Using the above results of interface energies we could determine the equilibrium crystal shape of the SrTe precipitates in PbTe host matrix from Wulff construction [1] using the Wulffman program [2]. The equilibrium crystal structure generated by the program is the Wulff shape [1].

Wulff construction is a method for determining the equilibrium shape of a crystal of fixed volume inside a different phase that minimizes the total interface energy. For a given set of interface energies $\gamma(n)$ where n is the interface orientation, the Wulff shape of the crystal from Wulff construction has the orientations that possess the lowest interface energies. Using the interface energies calculated from first principles DFT calculations, the shape of the SrTe precipitate in the PbTe matrix obtained from the Wulffman program [2] is shown in Fig. 6.3.

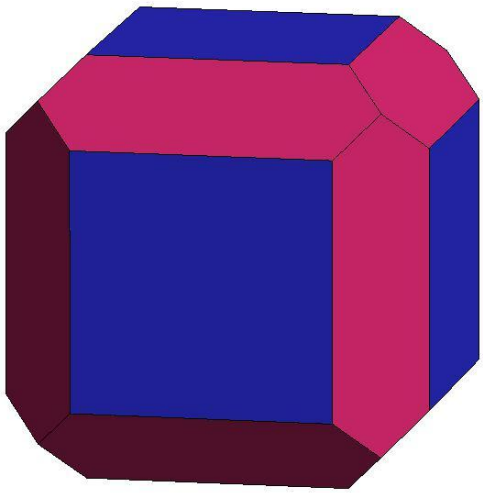

Figure 6.3: Wulff shape of SrTe precipitate in PbTe host matrix determined using the Wulffman program.

We could see that only the two lowest interface energies [100] and [110] play a role in determining the shape of SrTe precipitates in PbTe matrix. The [111] orientation has a significantly higher interface energy compared to the other two interfaces. Hence the minimum equilibrium crystal shape of SrTe precipitates does not have the [111] facets and it is a polyhedron.

Now we determine the band alignment of the material at the semiconductor heterojunction and also develop a relation between the interface energies and the valence band offset at the heterojunction of PbTe/SrTe alloys.

6.3 Semiconductor heterostructures

In a semiconductor heterostructure, two different semiconductors are brought into physical contact. These heterojunction devices find wide applications in most of the day-to-day solid state electronic devices. There are two main parameters that determine the performance of these devices namely the electronic band discontinuities and the built-in potentials. In these devices the carrier transport is either along the interface (MOSFETs) or across the interface (LEDs, LASERs). At the semiconductor heterojunction, there is an offset in the valence and conduction bands because of the presence of two different semiconductors with dissimilar energy bandgaps leading to band discontinuities. Heterojunction built-in potential arises because of band bending at the interface. At the junction, there is a sharp change in the band energies from one material to another, leading to local imbalance in the charge neutrality. These local changes in the energy offset are observed as energy band bending. The energy band offsets at the heterojunction have a major impact on the mobility of charge carriers. The lower the band offset, more easily the carriers could move across the interface leading to good carrier mobility.

6.4 Types of semiconductor heterojunctions

Based on the line–ups of the conduction, valence bands and the alignment of the forbidden energy bandgap, the heterostructures are classified into three different types as shown in Fig. 6.4 [3]. Type I alignment is the most common alignment in many semiconductor heterostructures. It is also called as the straddled or nested alignment where the bandgap of one material is completely contained within the bandgap of the other material. Type II alignment is also known as the staggered alignment where either the conduction or valence band of a semiconductor lies outside the bandgap of the other i.e. energy bandgap of one material is partially contained within the energy gap of the other. The most extreme type of alignment is the broken-gap alignment

(Type III) where both the conduction and valence bands do not overlap i.e. energy bandgaps are not contained.

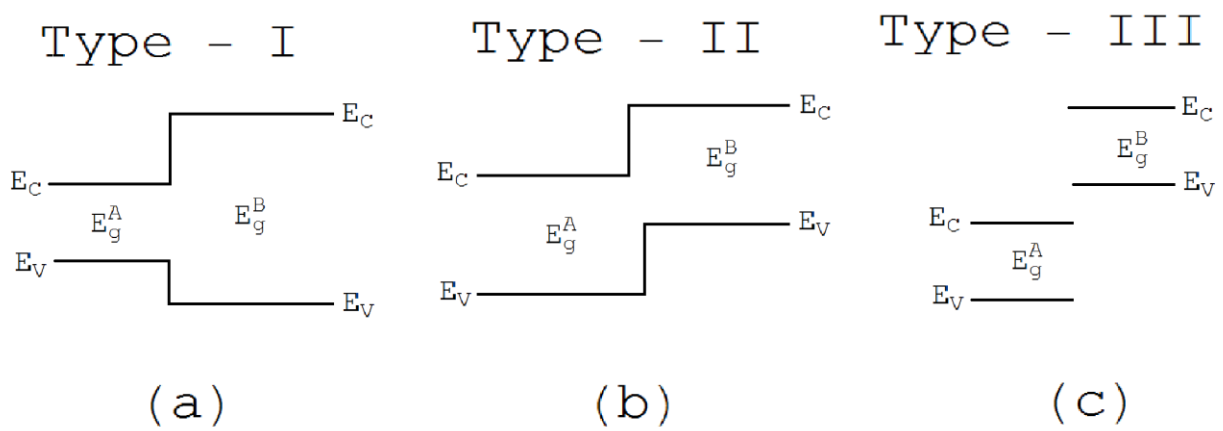

Figure 6.4: Types of Energy band line-ups.

where E_C and E_V are the energies of the conduction and valence bands. E_g^A and E_g^A are the forbidden energy bandgaps of material A and B respectively. As discussed, at the heterojunction the energies of conduction and valence band change and the magnitude of this change is critical for the semiconductor heterostructure devices [3]. The quality of heterojunctions depends on match between two semiconductor lattices and the electronic properties. The transport properties in heterojunction devices are controlled by the electronic band profiles at the heterojunction, the conduction and valence band discontinuities that accommodate the difference in bandgap of the materials [4].

6.5 Formulation of band-lineup problem

The band-lineup in a semiconductor heterojunction could be explained by considering two lattice matched semiconductors A and B like PbTe and SrTe (experimental lattice parameters of PbTe and SrTe are 6.46 Å and 6.66 Å at 300 K respectively [5]). They have different energy bandgaps ($E_g^{PbTe} = 0.13\ eV\ and\ E_g^{SrTe} = 1.472\ eV\ at\ 0\ K$) and are linked at the interface. Because of the

energy bandgap discontinuity, the conduction and valence bands are also discontinuous as shown in Fig. 6.5 [6].

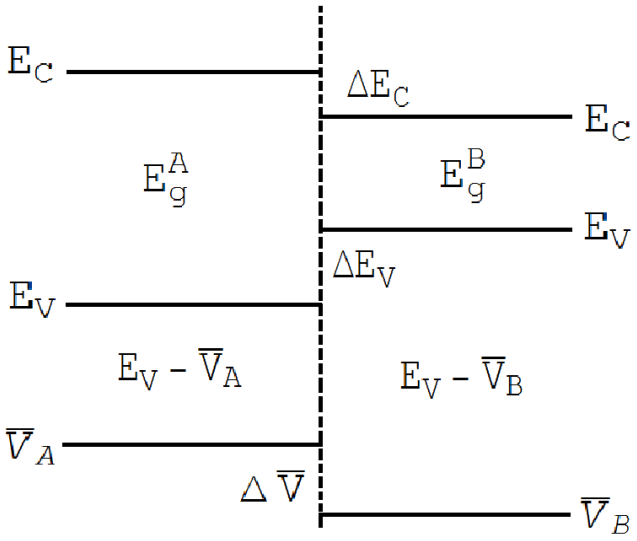

Figure 6.5: Schematic representation of band line-up formulation between semiconductors.

where $\bar{V}_A$ is the reference or average electrostatic potential of semiconductor A, $\bar{V}_B$ is the reference or average electrostatic potential of semiconductor B, $\Delta\bar{V}$ is the difference in average electrostatic potentials between A and B, $\Delta E_V, \Delta E_C$ are the valence and conduction band offsets of the semiconductors at the heterojunction. The energy band bending on the either side of the interface is neglected and flat bands are assumed because our primary area of focus is few atomic distances on both the sides of the heterojunction and at these length scales the above assumption holds good [6]. The difference in average electrostatic potential is calculated by performing the bandstructure calculation with both semiconductors joined at the junction so that the electrostatic potentials of the materials are expressed with respect to the same reference and hence it is easier to evaluate the $\Delta\bar{V}$.

6.6 Self-consistent first principles calculations

Many theoretical methods have been proposed to predict and calculate the heterojunction energy band offsets in semiconductor heterostructures. First principles DFT calculations are widely used in this study. The ground state energy and stable structure of the system are determined from DFT calculations using VASP by relaxing the system. The periodicity of the system is maintained in which the layers of two semiconductor materials are periodically repeated as shown in Fig. 6.6.

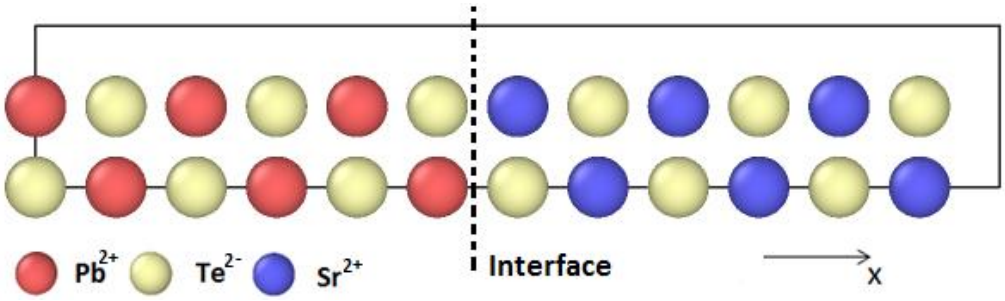

Figure 6.6: Semiconductor heterojunction (PbTe/SrTe heterostructure) with [100] interface.

Adequate planes of atoms are considered to ensure the separation between adjacent interfaces to avoid interactions between two interfaces. In our case, six planes of atoms are considered for each semiconductor. The potentials and the charge densities converge rapidly to the bulk values away from the interface. The values of the average potentials are determined in the bulk region. To determine the band–lineup across the interface, we are interested in the potential perpendicular to the interface [6]. The one-dimensional variation of potential is sufficient to determine the difference in average electrostatic potential. The other two co-ordinates can be removed by averaging in planes parallel to the interface [7]. The expression for average potential along the direction perpendicular to the interface is given by

$$\bar{V}(x) = \frac{1}{S}\int_{S} V(x,y,z)\, dy\, dz$$

where S is the area of for a unit cell in the y–z plane of the interface. The above expression gives the one–dimensional function which incorporates the periodic variations in the direction perpendicular to the interface. The positions of the average potentials in the bulk like regions are shifted with respect to one another, providing the value for $\Delta\bar{V}$ which depends on the charge density of the heterojunction. The variation of plane-averaged potential for the PbTe/SrTe system is shown in Fig. 6.7.

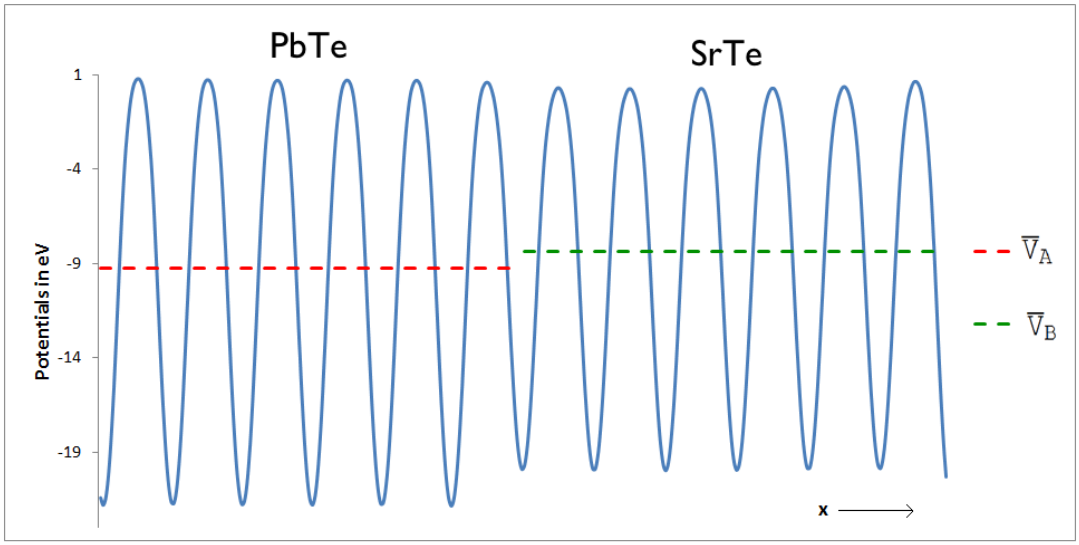

Figure 6.7: Variation of plane averaged potential along the direction perpendicular to the interface.

Now the valence band offset of the material is given by the following expression,

$$VBO = \Delta\bar{V} + \Delta E_V$$

$\Delta E_V = (E_V^A - \bar{V}_A) - (E_V^B - \bar{V}_B)$ [7] is the difference of the valence band maximum between two semiconductors and $\Delta\bar{V}$ is the potential line–up which is obtained from the difference between the plane averaged potentials of two semiconductor materials. The valence band offset at the PbTe and SrTe semiconductor heterojunction for different interface orientations is shown in Table 6.2

Table 6.2: Valence band offset at PbTe/SrTe semiconductor heterojunction

Interface Orientation	Valence band offset in eV
[100]	0.264
[110]	0.391
[111]	0.469

We see that the valence band offset is around 0.264 eV for the [100] interface and it gradually increases for [110] and [111] interfaces. This low value of valence band offset is the primary reason for a good electronic band alignment between PbTe and SrTe materials. As the valence band offset between the SrTe precipitates and PbTe host matrix is low, the charge carrier transport across the two phases is easier with very less charge scattering at the interface leading a good charge carrier mobility thereby enhancing the performance of $Pb_{1-x}Sr_xTe$ thermoelectric alloys [5].

6.7 Relation between interface energy and band offset

In this section we have tried to develop a relation between interface energy ($\Delta\varepsilon$) in eV and the valence band offset between PbTe and SrTe semiconductors in eV. The valence band offset and interface energy for [100], [110] and [111] orientations from DFT calculations are compared in Fig. 6.8. We could see that the interface energies and the valence band offset for our material (PbTe and SrTe) are directly related. The higher the interface energy at the heterojunction, the larger is the valence band offset.

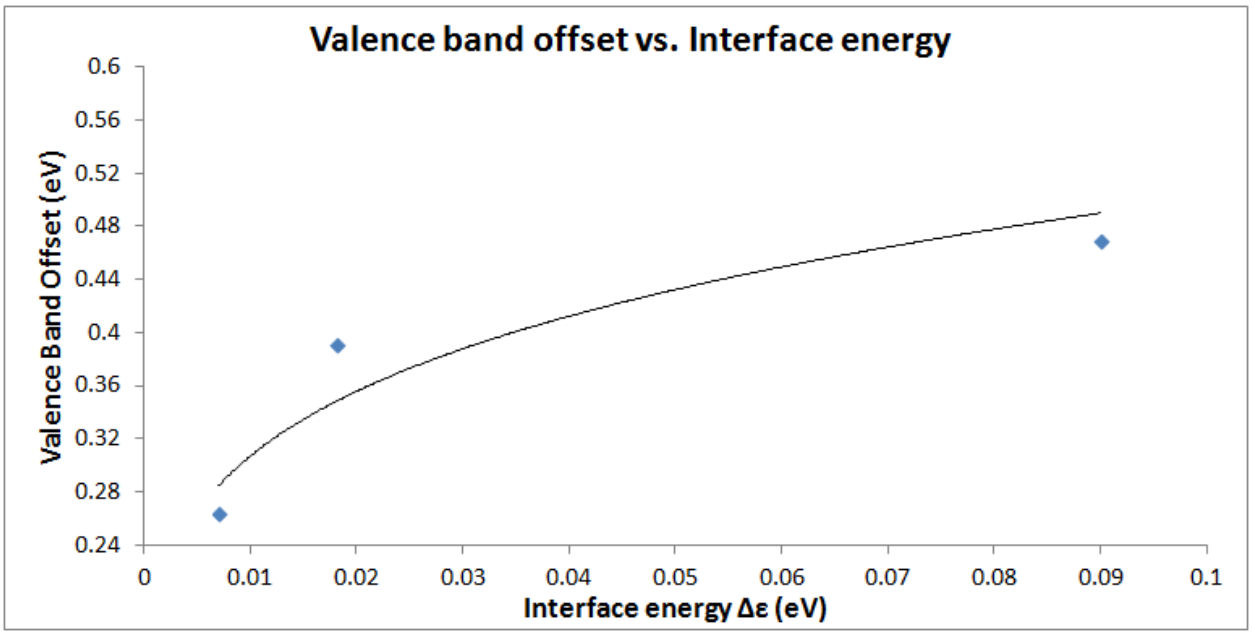

Figure 6.8: Comparison of valence band offset and interface energy for different interface orientations.

We attempted to fit an expression for the valence band offset and interface energy between PbTe and SrTe. The expression is given as,

$$VBO = 0.8181\Delta\varepsilon^{0.213}$$

where VBO is the valence band offset at the semiconductor heterojunction in eV and $\Delta\varepsilon$ is the interface energy in eV. The lowest interface energy is the [100] interface and from the Wulff shape generated we could see that the prominent facet of the equilibrium crystal shape is [100] and the corresponding valence band offset is 0.264 eV. Thus $Pb_{1-x}Sr_xTe$ thermoelectric material has a low valence band offset leading to good charge carrier mobility across the two different materials of the alloy i.e. there is minimal charge carrier scattering at the PbTe/SrTe interfaces leading to a good thermoelectric performance.

6.8 Conclusion

In this chapter we discussed the procedure involved in determining the interface energy between SrTe precipitate and PbTe host matrix for different interface orientations using first principles

DFT calculations. We also evaluated the evolution of interface energy as a function of number of planes of atoms used in the calculations. The equilibrium shape of the SrTe precipitates inside the PbTe host matrix through the Wulff construction using the Wulffman program was also obtained. We determined the valence band offset at the PbTe/SrTe semiconductor heterojunction for different interface orientations and finally we arrived at an expression that relates the valence band offset of PbTe/SrTe at the heterojunction and the interface energy. The lowest interface energy has the lowest valence band offset. The equilibrium shape of the SrTe precipitates in the PbTe host matrix has a majority of [100] facets and has a low valence band offset of 0.264 eV at the semiconductor heterojunction facilitating the charge carrier mobility across the material in the presence of SrTe precipitates, thereby, enhancing the thermoelectric performance.

6.9 References

1. G.Wulff, Z. Kristallogr, Mineral. **34**, 449 – 530 (1901).
2. A.R. Roosen, R.P. McCormack, W.C. Carter, Wulffman: A tool for the calculation and display of crystal shapes. *Computational Materials Science* **11**, 16 – 26 (1998).
3. L.J. Brillson, Surfaces and Interfaces of electronic materials. Wiley – VCH, Weinheim (2010).
4. M. Peressi, N. Binggeli, A. Baldereschi, Band engineering at interfaces: theory and numerical experiments. *Journal of Physics D: Applied Physics* **31**, 1273 – 1299 (1998).
5. K. Biswas, J. He, I.D. Blum, C.I. Wu, T.P. Hogan, D.N. Seidman, V.P. Dravid, M.G. Kanatzidis, High – performance bulk thermoelectric with all – scale hierarchical architectures. *Nature* **489**, 414 – 418 (2012).
6. A. Franciosi, C.G. Van de Walle, Heterojunction band offset engineering. *Surface Science Reports* **25**, 1 – 140 (1996).
7. J.V. Pezold, P.D. Bristowe, Atomic structure and electronic properties of the GaN/ZnO (0001) interface. *Journal of Materials Science* **40**, 3051 – 3057 (2005).

7 Conclusions and future work

7.1 Thesis contribution

In this work we determined the temperature dependence of electronic properties of PbTe like energy bandgap, effective masses of charge carriers from first principles DFT calculations. We incorporated the temperature effects on the structural properties of the material like lattice thermal expansion and distortion of Pb^{2+} ions to get the above results. The calculated electronic properties were used to determine the charge carrier scattering relaxation time at different temperatures which is an important parameter in determining the transport properties of the thermoelectric material. We also studied the effect of interfaces on charge carrier mobility in thermoelectric materials. The charge carrier mobility across the material in the presence of SrTe interface was studied by determining the interface energies and the valence band offset at the semiconductor heterojunction. A relation between interface energies and the band alignment at heterojunction was developed. We also used the interface energies of different interface orientations to determine the equilibrium crystal shape of SrTe precipitates in the PbTe host matrix from Wulffman construction.

7.2 Future work

This work has the potential to be extended in multiple directions.

1. The results from our DFT calculations and the total carrier scattering relaxation time could be used in determining the transport properties of the materials like Seebeck coefficient and electrical conductivity at different temperatures.

2. The thermal conductivity of the thermoelectric material could be obtained from molecular dynamics simulations. Using the computed results we could determine the zT of the material.
3. From the interface energy calculations we could evaluate the material properties like solubility limit of Sr in PbTe.
4. Based on our first principles DFT results, we could also determine the number density, shape and size of the precipitates using KMC algorithms.